Meteoritics & Planetary Science 39, Nr 9, 1517–1553 (2004)
Abstract available online at http://meteoritics.org

Fine-grained, spinel-rich inclusions from the reduced CV chondrites Efremovka and Leoville: I. Mineralogy, petrology, and bulk chemistry

Alexander N. KROT,[1*] Glenn J. MACPHERSON,[2] Alexander A. ULYANOV,[3] and Michail I. PETAEV[4]

[1]Hawai'i Institute of Geophysics and Planetology, School of Ocean and Earth Science and Technology, University of Hawai'i at Manoa, Honolulu, Hawai'i 96822, USA
[2]Smithsonian Institution, Department of Mineral Sciences, NHB 119, Washington D.C. 20560, USA
[3]M. V. Lomonosov Moscow State University, Moscow 119992, Russia
[4]Harvard-Smithsonian Center for Astrophysics and Department of Earth and Planetary Sciences, Harvard University, Cambridge, Massachusetts 02138, USA
[*]Corresponding author. E-mail: sasha@higp.hawaii.edu

(Received 24 February 2003; revision accepted 28 June 2004)

Abstract–Fine-grained, spinel-rich inclusions in the reduced CV chondrites Efremovka and Leoville consist of spinel, melilite, anorthite, Al-diopside, and minor hibonite and perovskite; forsterite is very rare. Several CAIs are surrounded by forsterite-rich accretionary rims. In contrast to heavily altered fine-grained CAIs in the oxidized CV chondrite Allende, those in the reduced CVs experienced very little alteration (secondary nepheline and sodalite are rare). The Efremovka and Leoville fine-grained CAIs are ^{16}O-enriched and, like their Allende counterparts, generally have volatility fractionated group II rare earth element patterns. Three out of 13 fine-grained CAIs we studied are structurally uniform and consist of small concentrically zoned nodules having spinel ± hibonite ± perovskite cores surrounded by layers of melilite and Al-diopside. Other fine-grained CAIs show an overall structural zonation defined by modal mineralogy differences between the inclusion cores and mantles. The cores are melilite-free and consist of tiny spinel ± hibonite ± perovskite grains surrounded by layers of anorthite and Al-diopside. The mantles are calcium-enriched, magnesium-depleted and coarser-grained relative to the cores; they generally contain abundant melilite but have less spinel and anorthite than the cores. The bulk compositions of fine-grained CAIs generally show significant fractionation of Al from Ca and Ti, with Ca and Ti being depleted relative to Al; they are similar to those of coarse-grained, type C igneous CAIs, and thus are reasonable candidate precursors for the latter. The fine-grained CAIs originally formed as aggregates of spinel-perovskite-melilite ± hibonite gas-solid condensates from a reservoir that was ^{16}O-enriched but depleted in the most refractory REEs. These aggregates later experienced low-temperature gas-solid nebular reactions with gaseous SiO and Mg to form Al-diopside and ±anorthite. The zoned structures of many of the fine-grained inclusions may be the result of subsequent reheating that resulted in the evaporative loss of SiO and Mg and the formation of melilite. The inferred multi-stage formation history of fine-grained inclusions in Efremovka and Leoville is consistent with a complex formation history of coarse-grained CAIs in CV chondrites.

INTRODUCTION

Ca-Al-rich inclusions (CAIs) experienced long and complex evolutionary histories before their accretion into chondritic parent bodies 4.56 Ga ago (e.g., MacPherson et al. 1988; Davis et al. 1991; Sylvester et al. 1992, 1993; MacPherson and Davis 1993; Simon et al. 1991, 1998; Simon and Grossman 1997; Grossman et al. 2000), but their ultimate precursor materials are thought by most workers to have originated by nebular condensation. In most cases, however, there is little direct evidence of that condensation process. One exception is the class of CAIs that possess volatility-fractionated trace element patterns in which the most refractory elements are substantially depleted. Such patterns were first identified by Tanaka and Masuda (1973) in a fine-grained, spinel-rich CAI from Allende, and it was observed subsequently that similar inclusions in CV chondrites commonly are characterized by such trace element patterns. Boynton (1975) and, later, Davis and Grossman (1979) showed that these so called group II (Martin and Mason 1974)

trace element patterns can only be formed by condensation; they cannot be vaporization residues. Thus, CAIs with group II trace element patterns remain one of the strongest kinds of evidence for condensation in the early solar nebula.

For the first ~20 yr after their recognition, most CAI research was done on the exceptionally large (often >5 mm in apparent diameter) examples from the CV (Vigarano-type) carbonaceous chondrites, especially Allende, the fall of which (in 1969, in Mexico) provided a huge amount of material. Much of this work naturally focused on the "coarse-grained" CAIs, the constituent phases of which are easily studied by optical microscopy and can be split into mineral separates for detailed isotopic studies. Such is not the case for the fine-grained inclusions, the small grain sizes of which (generally <10 μm) require electron microscopy for petrologic study. Even the advent of routine use of the ion microprobe for CAI analysis (e.g., Hutcheon 1982) did little to facilitate the study of fine-grained inclusions; for example, their individual phases are too small for effective ion probe analysis (until very recently) of magnesium isotopes in the search for extinct ^{26}Al. Finally, the primary mineralogy of fine-grained inclusions in Allende has been extensively replaced by the alkali- and iron-rich secondary mineralization that is prevalent throughout Allende (e.g., Grossman and Ganapathy 1976; Cohen 1981; Kornacki 1981, 1982, 1984; MacPherson and Grossman 1982; Kornacki and Cohen 1983; Kornacki and Fegley 1984; Fegley et al. 1984; Kornacki and Wood 1984, 1985; Hashimoto and Grossman 1985; McGuire and Hashimoto 1989; Krot et al. 1995, 1998). As a result, little detailed work has been done since the late 1970s and early 1980s to characterize and understand the genesis of this important variety of CAIs. However, two recent changes suggest that it is time to re-examine fine-grained, spinel-rich CAIs for the unique clues they hold to early solar system processes. First, advances in ion microprobe analytical technology now make it possible to analyze isotopic systems (especially oxygen), and with much higher spatial resolution, in situ in thin sections that previously could not be measured. The second advance is the recognition that the reduced-subgroup CV chondrites (e.g., Vigarano, Efremovka, and Leoville) contain very little of the Allende-style secondary mineralization, and hence, their CAIs more clearly preserve their original properties (Ulyanov 1984; Boynton et al. 1986; Wark et al. 1986).

Therefore, we initiated systematic mineralogic, petrologic, and ion microprobe studies of a large collection of fine-grained, spinel-rich CAIs from the reduced chondrites Efremovka and Leoville. Our goals are to constrain the primary mineralogy and origin of fine-grained, spinel-rich inclusions in CV chondrites, understand their relationship with coarse-grained inclusions, determine the distribution of the group II REE signature within individual CAIs, and elucidate the nature of the oxygen isotopic pattern in these condensate CAIs. In this paper, we describe the mineralogy, petrology, and bulk major element chemistry of the CAIs; oxygen isotopic compositions and trace element abundances in these CAIs will be reported in separate papers.

ANALYTICAL PROCEDURES

Polished sections of the Efremovka and Leoville CAIs were studied using optical microscopy, backscattered electron (BSE) imaging, X-ray elemental area mapping, and electron probe microanalysis. BSE images were obtained with the JEOL JSM 5900LV and Zeiss DSM 962 scanning electron microscopes using a 15–20 kV accelerating voltage and 1–2 nA beam current. Electron probe microanalyses were performed with a Cameca SX-50 electron microprobe using 15 kV accelerating voltage, 10–20 nA beam current, beam size of ~1–2 μm, and wavelength dispersive X-ray spectroscopy. For each element, counting times on both peak and background were 30 sec (10 sec for Na and K; both elements were analyzed first). Matrix effects were corrected using PAP procedures. The element detection limits (2σ) with the Cameca SX-50 were (in wt%): 0.04 (K_2O), 0.07 (Cr_2O_3), 0.08 (Na_2O), and 0.09 (FeO). X-ray elemental maps with a resolution of 2–5 μm/pixel were acquired with five spectrometers of the Cameca microprobe operating at 15 kV accelerating voltage, 50–100 nA beam current and ~1–2 μm beam size. The Mg, Ca, and Al X-ray images were combined by using a RGB color scheme and ENVI (Environment for Visualizing Images) software to obtain false color maps. Bulk compositions of the CAIs and compositions of their core and mantle zones were measured using a ~15 × 15 μm rastered beam; between 70 and 400 analyses for each CAI were acquired along profiles uniformly covering a whole inclusion. For zoned inclusions, average analyses of cores and mantles were combined in weighted proportions as determined by measuring the respective areas in thin section; the area fractions were converted to volume fractions assuming spherical symmetry. We necessarily assumed that the thin sections cut through the centers of the inclusions; as a result, the volume fractions of the core regions are probably lower limits.

RESULTS

Descriptions

The fine-grained, spinel-rich inclusions we studied consist (Table 1) primarily of spinel, pyroxene that ranges in composition from Al-diopside to Al-Ti-rich diopside, anorthite, and melilite; hibonite and perovskite are accessory in some inclusions, and in rare cases, forsterite is present as well. Nepheline and sodalite are minor; hedenbergite,

Table 1. List of fine-grained, spinel-rich CAIs from the reduced CV chondrites Efremovka and Leoville.[a]

Chondrite	CAI#	hib	pv	sp	mel	an	nph	Al-di	fo	fo rim
Unzoned										
Efremovka	E101b-1	–	+	+	+	–	–	+	–	–
Efremovka	E46-a	–	+	+	+	–	tr	+	–	–
Leoville	L3535-5f	+	+	+	+	–	–	+	–	–
Zoned Melilite-rich										
Efremovka	E103a	+	+	+	+	+	tr	+	–	–
Efremovka	E67-1	–	+	+	+	+	tr	+	–	–
Leoville	L3536-1	–	+	+	+	+	–	+	–	+
Efremovka	E42	–	+	+	+	+	tr	+	–	+
Efremovka	E49-a[b]	–	+	+	+	+	–	+	–	–
Melilite-poor/free										
Efremovka	E51	–	+	+	tr	+	tr	+	tr	–
Efremovka	E14	–	+	+	tr	+	–	+	tr	+
Efremovka	E101b	–	–	+	–	+	–	+	tr	+
Leoville	L3535-5	–	+	+	–	+	tr	+	tr	+
Efremovka	E71	–	+	+	–	+	–	+	–	–

[a]Al-di = Al-diopside; an = anorthite; fo = forsterite; hib = hibonite; mel = melilite; nph = nepheline; pv = perovskite; sp = spinel; tr = traces.
[b]Compound inclusion; only the mineralogy of the fine-grained inclusion is listed.

andradite, and ferrous olivine were not observed. Most of the inclusions are irregularly shaped; the only exception is the ellipsoidal object E101b. Probably owing to the high degree of parent body compaction exhibited overall by both the Leoville and Efremovka meteorites (e.g., MacPherson and Krot 2002), none of the inclusions we studied shows the high degree of porosity observed in Allende fine-grained, spinel-rich CAIs (e.g., Grossman et al. 1975; Hashimoto and Grossman 1985).

Most of the inclusions (10 out of 13 studied) show a prominent concentrically zoned structure, defined by significant differences in modal mineralogy. In most of these, a melilite-pyroxene-rich and spinel-anorthite-depleted outer mantle encloses a melilite-pyroxene-poor and anorthite-spinel-rich core. More rarely, there is no melilite even in the mantle, but the proportion of pyroxene to anorthite to spinel is markedly different in the mantle than in the core. One of the zoned inclusions is a compound object, having a coarse-grained, melilite-rich (type A) CAI molded onto one outer surface.

The remaining three inclusions do not display such zoned structures and have uniform textures and mineralogy throughout; these tend to be smaller than the zoned inclusions.

At the micro scale, all of the fine-grained inclusions are aggregates of numerous small irregularly shaped nodules consisting of spinel ± hibonite ± perovskite, each of which is surrounded by thin and nearly monomineralic layers of Al-diopside, ±melilite, and ±anorthite.

Mineralogically Unzoned Inclusions

The three mineralogically unzoned, fine-grained inclusions are illustrated in Fig. 1. All are melilite-bearing and anorthite-free. Inclusion E101b-1 shows the typical multiple, closely-packed, irregularly shaped nodules of spinel, each surrounded successively by a relatively thick layer of melilite and a very thin layer of Al-diopside (Figs. 1a and 1b). (The nomenclature for Efremovka inclusions has led to some confusion that requires clarification here. Cut slabs of the meteorite were given numbers such as E101 and E49, and each slab may contain multiple CAIs. E101b-1 is not the same CAI as E101b. Slab E49 contained at least three CAIs that have been studied by different workers. The one studied here, E49-a, is not the same CAI as, e.g., one studied by El Goresy and Zinner [1994].) Spinel grains in the outer portion of the CAI contain higher abundances of tiny inclusions of perovskite than those in the central part. Inclusion E46-a contains more numerous and coarser perovskite crystals inside spinel nodules throughout the CAI, each again surrounded by melilite and Al-diopside layers, but in this case, the proportion of pyroxene to melilite is greater (Figs. 1c and 1d). Leoville inclusion L3535-5f contains abundant hibonite intergrown with spinel and perovskite in the nodule cores, each surrounded by a thin layer of melilite and a slightly thicker layer of Al-diopside (Figs. 1e and 1f).

Mineralogically Zoned Inclusions

The mineralogically zoned, fine-grained inclusions vary continuously from melilite-rich (>5–10 vol%) to melilite-free. All contain abundant anorthite, and many are surrounded by forsterite-rich accretionary rims. The zoned structure is easily visible with the unaided eye on cut meteorite slices, but for our purposes, it is best illustrated in X-ray elemental area maps, either individual elemental maps of Ca, Al, and Mg or in composite Ca Kα (green) + Mg Kα (red) + Al Kα (blue) maps (Figs. 2–10). The composite maps, in particular,

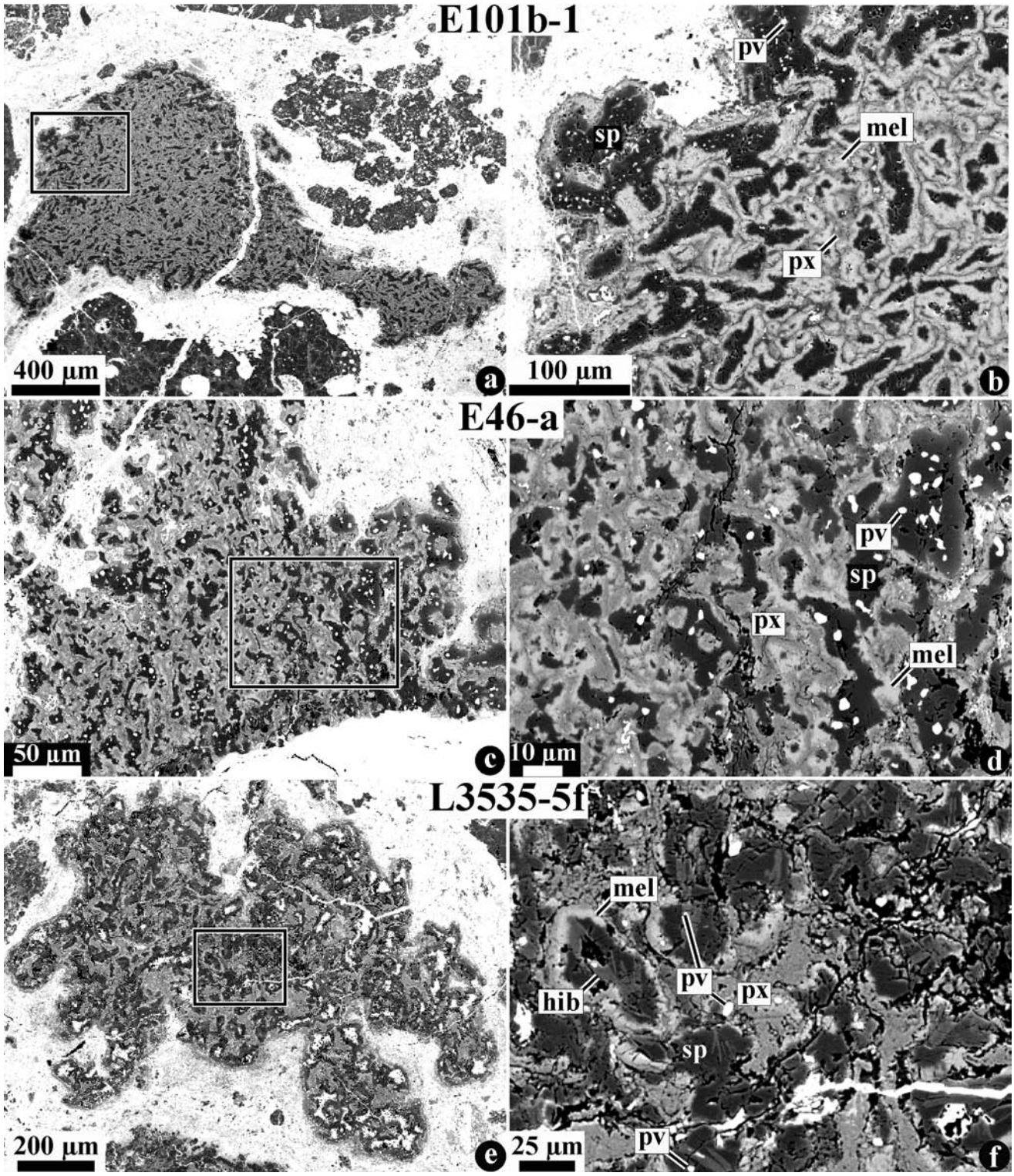

Fig. 1. BSE images of the mineralogically unzoned, fine-grained, spinel-rich inclusions E101b-1 (a, b) and E46-a (c, d) from Efremovka and L3535-5f (e, f) from Leoville. The rectangular regions outlined in (a), (c), and (e) are shown in detail in (b), (d), and (f), respectively; see text for details. The CAIs consist of closely packed, irregularly shaped spinel ± perovskite ± hibonite bodies surrounded by melilite and Al-diopside; hib = hibonite; mel = melilite; pv = perovskite; px = Al-diopside; sp = spinel.

emphasize the Ca-poor, Al-Mg-rich cores and Ca-rich, Al-Mg-poor mantles. In some cases, the structure is more complicated than just a core and mantle; sub-units within the mantle or core can be recognized. In all cases, the core-mantle boundaries are somewhat diffuse.

Melilite-Rich Inclusions

The Efremovka CAI E103a has a typical and relatively simple calcium (melilite)-poor core/calcium (melilite)-rich mantle structure (Figs. 2a and 2b). The Ti Kα X-ray map (Fig. 2d) reveals that the core can be further subdivided into a Ti-enriched inner part and a Ti-poor outer part. The nodules in the inner core are 10–20 μm in apparent diameter and contain centers of intergrown spinel + hibonite and, in some cases, perovksite. These nodules are surrounded by thin (<5 μm) successive layers of melilite, anorthite, and Al-diopside (Fig. 2e). The melilite layer varies in thickness and is locally discontinuous; its contact with the underlying spinel is highly irregular and, in places, scalloped, suggesting that it is replacing the spinel. In turn, the melilite is embayed and replaced by the overlying anorthite. Finally, the anorthite is overlain by aluminous diopside; however, this relationship is not as consistent as the other two just noted. There are many places in this and in other CAIs where the pyroxene overlies melilite directly. The reader should note that these texturally observed reactions are repeated consistently throughout the population of the fine-grained inclusions we studied and, thus, are fundamental to understanding the petrogenesis of these CAIs (see Discussion section). Two varieties of hibonite are observed in the core of E103a: low-Ti and high-Ti (0.5 wt% and 5.1 wt%,

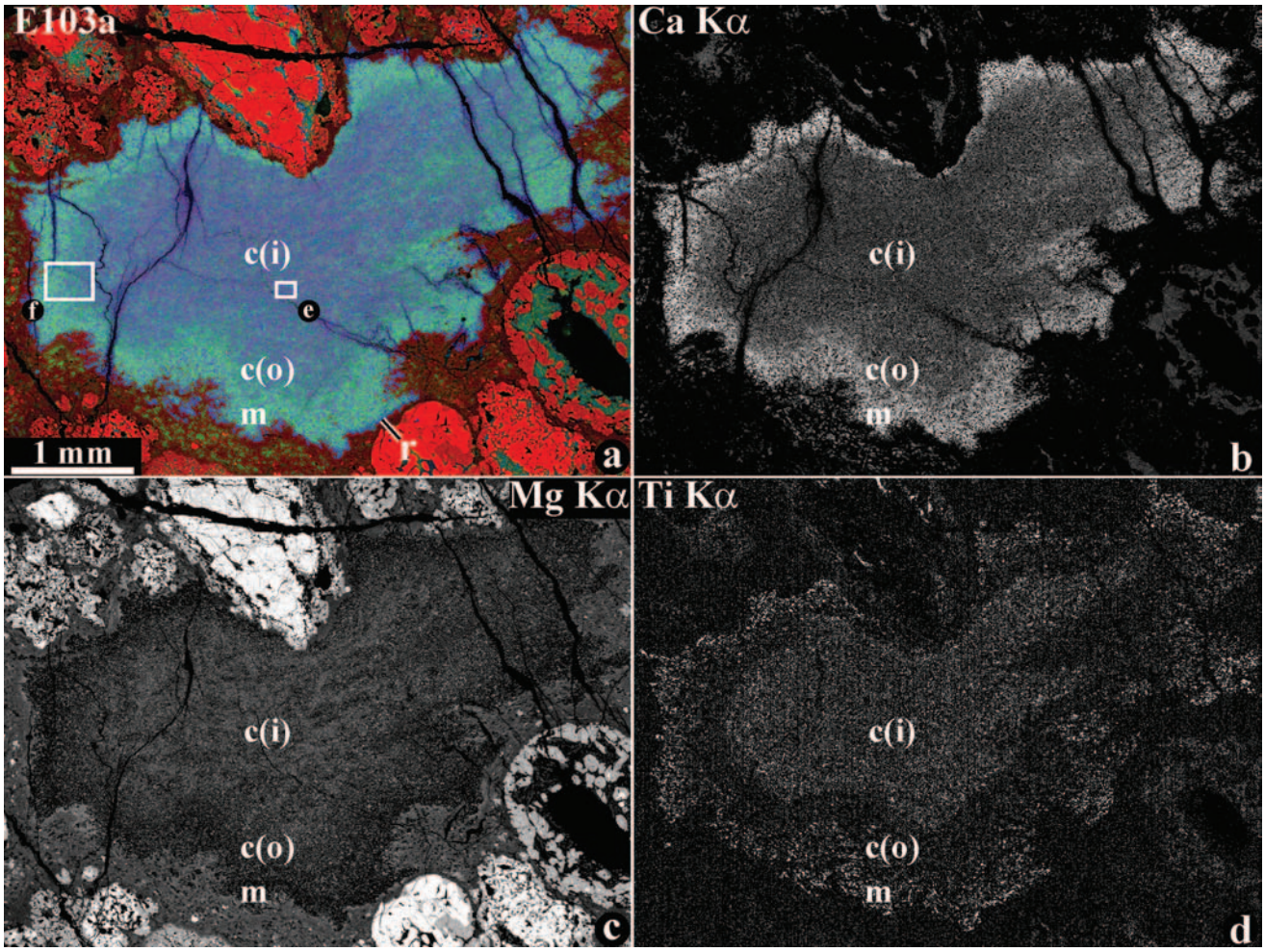

Fig. 2. Zoned, fine-grained, spinel-rich CAI E103a from Efremovka: a) combined X-ray elemental map; b, c, and d) individual X-ray element area maps for Ca (b), Mg (c), and Ti Kα (d); see text for details. The CAI has a Ca-poor core consisting of spinel, hibonite, perovskite, anorthite, Al-diopside, and minor melilite. Variations in brightness in the Ti Kα map reflect variations in distribution of hibonite and perovskite and distinguish a Ti-rich inner core and a Ti-poor outer core. The inclusion's Ca-rich mantle is made of spinel, hibonite, melilite, perovskite, and minor Al-diopside. The CAI is surrounded by a spinel-hibonite-rich rim; an = anorthite; hib-LT = low-Ti hibonite; hib-HT = high-Ti hibonite; c(i) = inner core; c(o) = outer core; m = mantle; r = rim; the other abbreviations are as used previously.

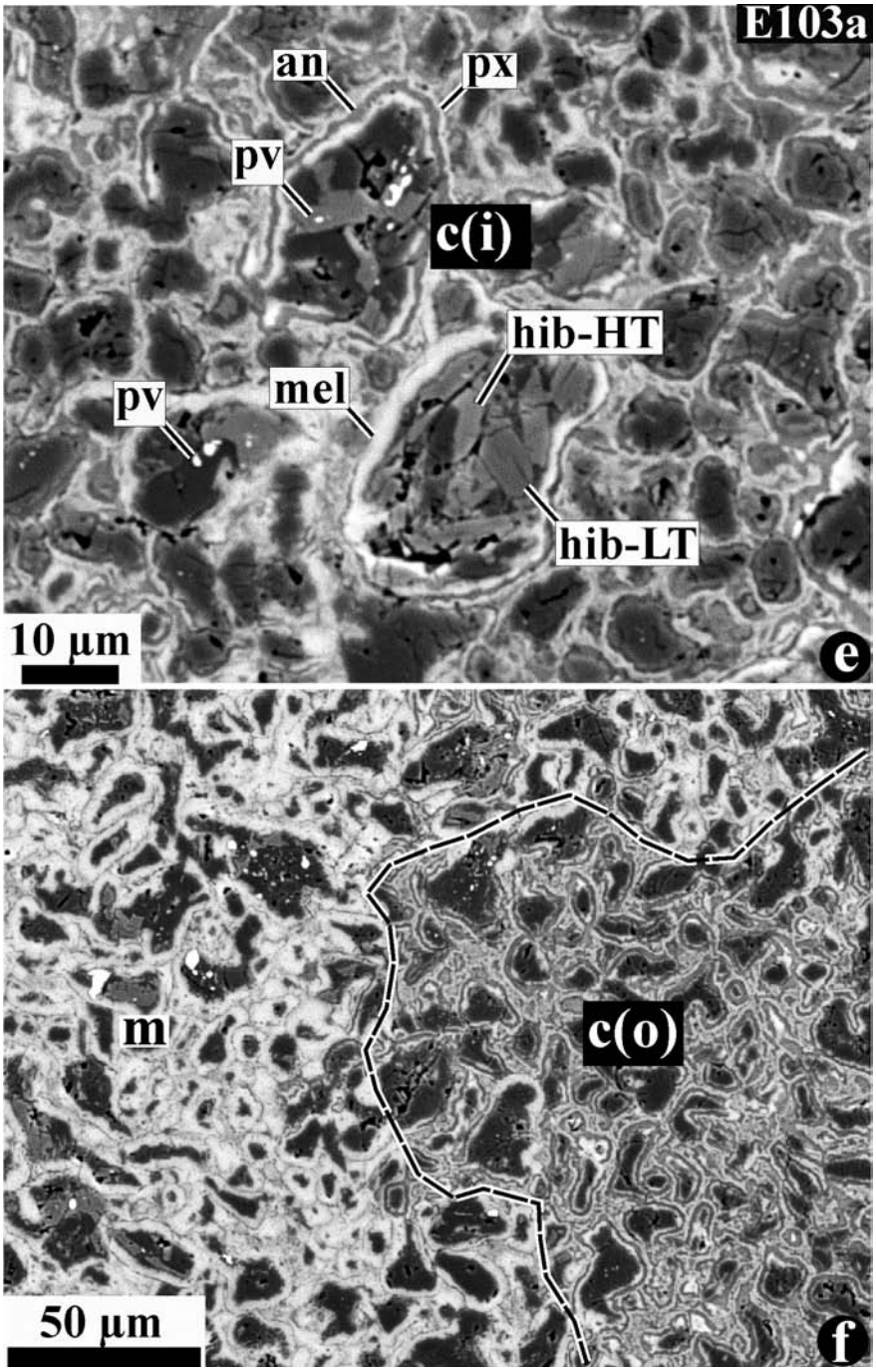

Fig. 2. *Continued.* Zoned, fine-grained, spinel-rich CAI E103a from Efremovka: e and f) BSE images of the regions outlined and labeled in (a); see text for details. The CAI has a Ca-poor core consisting of spinel, hibonite, perovskite, anorthite, Al-diopside, and minor melilite. Variations in brightness in the Ti Kα map reflect variations in distribution of hibonite and perovskite and distinguish a Ti-rich inner core and a Ti-poor outer core. The inclusion's Ca-rich mantle is made of spinel, hibonite, melilite, perovskite, and minor Al-diopside. The CAI is surrounded by a spinel-hibonite-rich rim; an = anorthite; hib-LT = low-Ti hibonite; hib-HT = high-Ti hibonite; c(i) = inner core; c(o) = outer core; m = mantle; r = rim; the other abbreviations are as used previously.

respectively; see Mineral Compositions section and Table 2), in some cases, within a single spinel-rich nodule (Fig. 2e). Perovskite is heterogeneously distributed but, where present, can be enclosed within both spinel and hibonite. The outer core is texturally and mineralogically similar to the inner core but contains less hibonite and perovskite (Figs. 2d and 2f). The CAI mantle is distinguished by thicker layers of melilite (Fig. 2f) that enclose the spinel-hibonite nodules and the thinner layers of Al-diopside, relative to the inner and outer core. Small grains of perovskite are scattered

Table 2. Representative microprobe analyses of spinel in fine-grained, spinel-rich CAIs from Efremovka and Leoville.

			E103a		E67-1		L3536-1	E42	E49-a[a]			E51	E14	E101b	L3535-5
Ox\CAI	E101b-1	L3535-5f	core	mantle	core	rim	core	core	core	mantle	FTA[b]	core	core	core	core
SiO_2	0.15	0.16	0.14	0.13	0.05	0.16	<0.03	0.19	0.23	0.17	0.13	0.28	0.14	0.16	0.05
TiO_2	0.18	0.09	0.28	0.23	0.45	0.25	0.16	0.08	0.42	0.20	0.13	0.18	0.21	0.33	0.32
Al_2O_3	71.3	71.9	71.3	68.7	71.4	69.6	72.5	70.5	70.8	72.1	71.5	72.0	70.0	71.1	73.0
Cr_2O_3	0.38	0.14	0.11	0.17	0.31	0.12	0.07	0.78	1.2	0.21	0.16	0.22	1.3	0.57	0.15
FeO	0.84	2.1	0.09	7.7	0.17	5.5	<0.08	<0.08	1.1	0.41	0.14	1.1	1.6	0.32	0.17
MnO	<0.07	<0.07	<0.07	<0.07	<0.07	<0.07	<0.07	<0.07	<0.07	<0.07	<0.07	<0.07	<0.07	<0.07	<0.07
MgO	27.9	26.5	27.9	23.0	27.4	24.3	27.6	29.26	27.1	27.9	27.8	27.0	27.9	28.5	27.9
CaO	0.23	0.07	0.21	0.12	0.08	0.17	0.21	0.36	0.20	0.20	0.71	0.09	0.12	0.07	0.04
V_2O_3	n.a.[c]	n.a.	n.a.	n.a.	0.36	0.33	n.a.	n.a.	0.19	0.37	0.46	<0.06	n.a.	n.a.	n.a.
Total	101.0	101.0	100.1	100.0	100.2	100.4	100.5	101.2	100.9	101.2	100.6	100.9	101.3	101.0	101.6
Structural formulae based on 4 O															
Si	0.003	0.004	0.003	0.003	0.001	0.004	–	0.004	0.005	0.004	0.003	0.007	0.003	0.004	0.001
Ti	0.003	0.002	0.005	0.004	0.008	0.005	0.003	0.001	0.007	0.003	0.002	0.003	0.004	0.006	0.006
Al	1.981	2.005	1.991	1.985	1.994	1.986	2.012	1.954	1.971	1.988	1.985	2.000	1.953	1.971	2.006
Cr	0.007	0.003	0.002	0.003	0.006	0.002	0.001	0.015	0.022	0.004	0.003	0.004	0.024	0.011	0.003
Fe	0.017	0.042	0.002	0.157	0.003	0.111	–	–	0.021	0.008	0.003	0.021	0.032	0.006	0.003
Mn	–	–	–	–	–	–	–	–	–	–	–	–	–	–	–
Mg	0.982	0.934	0.986	0.840	0.967	0.875	0.967	1.026	0.953	0.973	0.974	0.949	0.985	1.000	0.969
Ca	0.006	0.002	0.005	0.003	0.002	0.004	0.005	0.009	0.005	0.005	0.018	0.002	0.003	0.002	0.001
V	–	–	–	–	0.007	0.006	–	–	0.004	0.007	0.009	–	–	–	–
Total	2.998	2.992	2.995	2.997	2.981	2.988	2.988	3.009	2.985	2.986	2.987	2.986	3.004	2.999	2.989

[a]Compound inclusion.
[b]FTA = fluffy type A CAI.
[c]n.a. = not analyzed.

throughout the mantle (Fig. 2f), just as in the core, but anorthite is absent from the mantle. The abundance of spinel is generally lower in the mantle than in the core but sharply increases toward the outermost CAI edge. Spinel in this "rim" is enriched in FeO (7.7 wt%) relative to that in the core and mantle (0.09 wt%).

Inclusion E67-1 has a more complex, multi-layered structure (Fig. 3) than E103a. Its Ca-poor core (Fig. 3b) can be subdivided into inner and outer parts that are relatively Mg-rich and Mg-poor compared with each other (Fig. 3c), although, not in comparison with the mantle. Both parts of the core contain abundant irregularly shaped spinel grains, each surrounded by a thick layer of anorthite and a thin layer of Al-rich pyroxene; a minor amount of nepheline is also present.

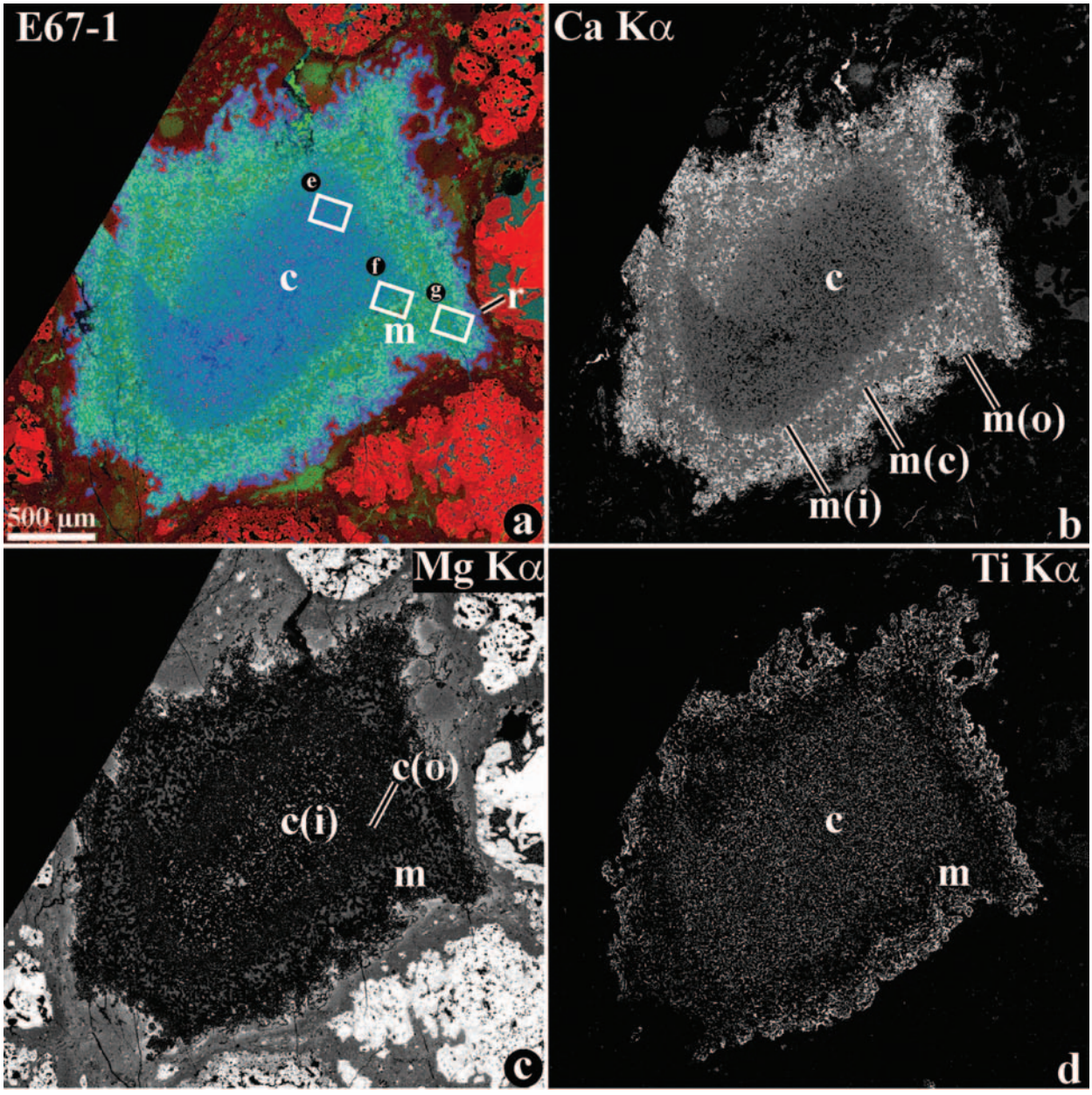

Fig. 3. Zoned, fine-grained, spinel-rich CAI E67-1 from Efremovka: a) combined X-ray elemental map (Mg = red, Ca = green, Al = blue); b, c, and d) individual X-ray element area maps for Ca (b), Mg (c), and Ti Kα (d); see text for details. The Ca-poor core can be subdivided into a Mg-rich inner part and a Mg-poor outer part. Both parts consist of spinel, anorthite, Al-diopside, and secondary nepheline. The inner core has higher abundance of spinel compared to the outer core. The mantle is Ca-rich overall, but it has three sublayers, of which the innermost and outermost are more Ca-rich than the intermediate one; all three consist of melilite, Al-diopside, anorthite, and spinel, but in different proportions. The CAI is surrounded by a spinel-rich rim; nph = nepheline; c(i) = inner core; c(o) = outer core; m(i) = inner mantle; m(c) = central mantle; m(o) = outer mantle; the other abbreviations are as used previously.

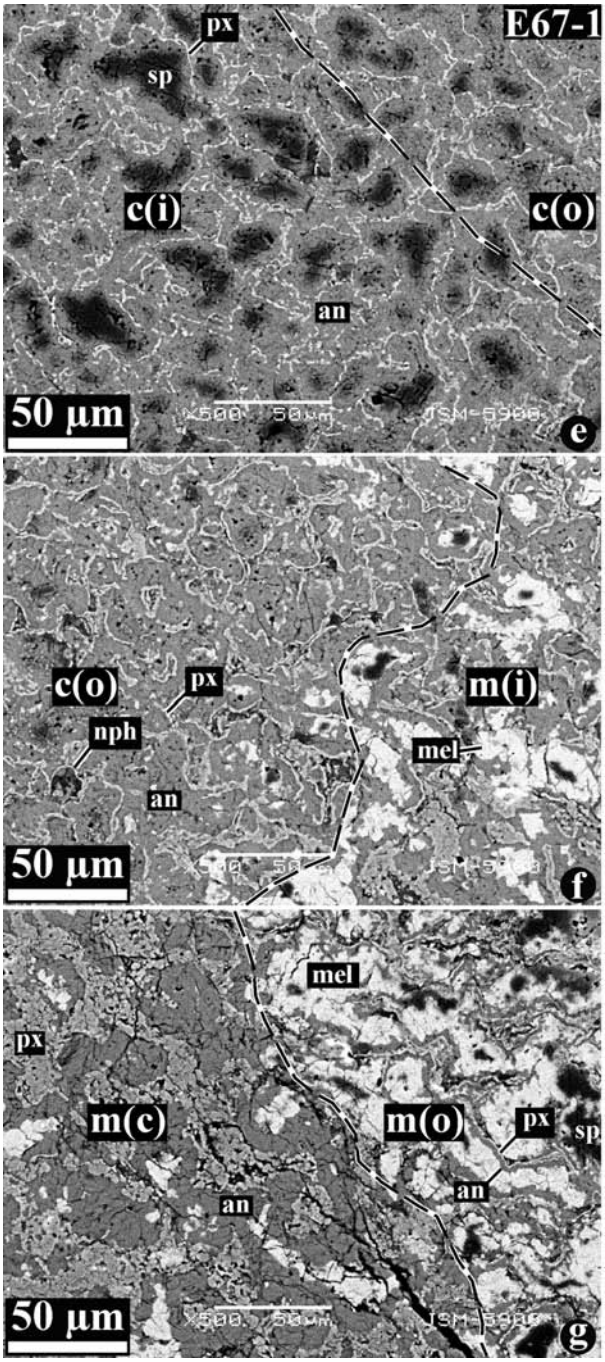

Fig. 3. *Continued.* Zoned, fine-grained, spinel-rich CAI E67-1 from Efremovka: e–g) BSE images of the regions outlined and labeled in (a); see text for details. The Ca-poor core can be subdivided into a Mg-rich inner part and a Mg-poor outer part. Both parts consist of spinel, anorthite, Al-diopside, and secondary nepheline. The inner core has higher abundance of spinel compared to the outer core. The mantle is Ca-rich overall, but it has three sublayers, of which the innermost and outermost are more Ca-rich than the intermediate one; all three consist of melilite, Al-diopside, anorthite, and spinel, but in different proportions. The CAI is surrounded by a spinel-rich rim; nph = nepheline; c(i) = inner core; c(o) = outer core; m(i) = inner mantle; m(c) = central mantle; m(o) = outer mantle; the other abbreviations are as used previously.

The abundance of spinel decreases from the inner core to the outer core (Figs. 3e and 3f). In the CAI mantle, the irregular spinel grains are enclosed in melilite, which, in turn, is surrounded by a layer of anorthite and a thick, continuous layer of Al-diopside (Figs. 3f and 3g). Based on the Ca distribution (Fig. 3b), the mantle itself has three zones: a Ca-rich inner part, a central region that is relatively Ca-depleted, and a Ca-rich outer zone. The central mantle zone is characterized by a lower abundance of melilite and higher abundance of anorthite than the inner and outer zones (Figs. 3f and 3g). The outermost part of the mantle contains the highest abundance of melilite, occurring as irregularly shaped compact objects enclosing spinel grains and surrounded by only thin layers of anorthite and Al-diopside (Fig. 3g). In this as in the other concentrically zoned, fine-grained CAIs, the boundaries between the various core and mantle layers are parallel to one another and to the CAI edge. The CAI is surrounded by an ill-defined, discontinuous, monomineralic spinel rim (Fig. 3a); the spinel is enriched in FeO (5.5 wt%) relative to that in the core and mantle (0.17 wt%).

Leoville inclusion L3536-1 has previously been studied by Mao et al. (1990), who showed it to have a group II REE pattern. Figures 4a–4d show a multi-layered overall structural zonation of the CAI that parallels the shape and boundary of this highly irregularly shaped inclusion; the multiple layers show up most vividly in the Ti Kα X-ray map (Fig. 4d). The numerous small and irregularly shaped spinel ± perovskite nodules in the core are markedly porous and follow the general pattern of being surrounded by successive layers of anorthite and Al-Ti-rich pyroxene that, in contrast, are not very porous (Fig. 4e). The thickness of the Al-diopside layer and the abundance of perovskite inclusions in spinel nodules both increase toward the outer part of the core, culminating in a particularly Ti-rich layer at the core-mantle interface (Fig. 4d). The mantle zone is composed of melilite, spinel, anorthite, and Al-diopside (Figs. 4f–4h). Textures in the inner part of the mantle do not follow the pattern seen in the CAIs described above because, in this case, the spinel nodules enclose melilite rather than being surrounded by it (Fig. 4g). The melilite + spinel nodules are surrounded by thin anorthite and thick Al-diopside layers (Fig. 4g). Moving outward through the CAI mantle, the abundance and grain-size of both melilite and Al-diopside increase, and the abundance of anorthite and spinel decreases (Figs. 4f–4h). In the outermost portion of the mantle, melilite forms nearly spinel-free massive regions surrounded only by Al-diopside (Fig. 4h). Finally, the CAI is surrounded by a discontinuous layer of spinel, a more continuous layer of Al-diopside, and a forsterite-rich accretionary rim (Figs. 4a and 4h).

Inclusion E42 is an irregularly shaped object with a relatively simple structure, having a well-defined Ca-poor core and Ca-rich mantle and a thin forsterite-rich accretionary rim (Fig. 5). The very spinel-rich core consists of irregularly shaped spinel nodules that enclose sparse tiny perovskite

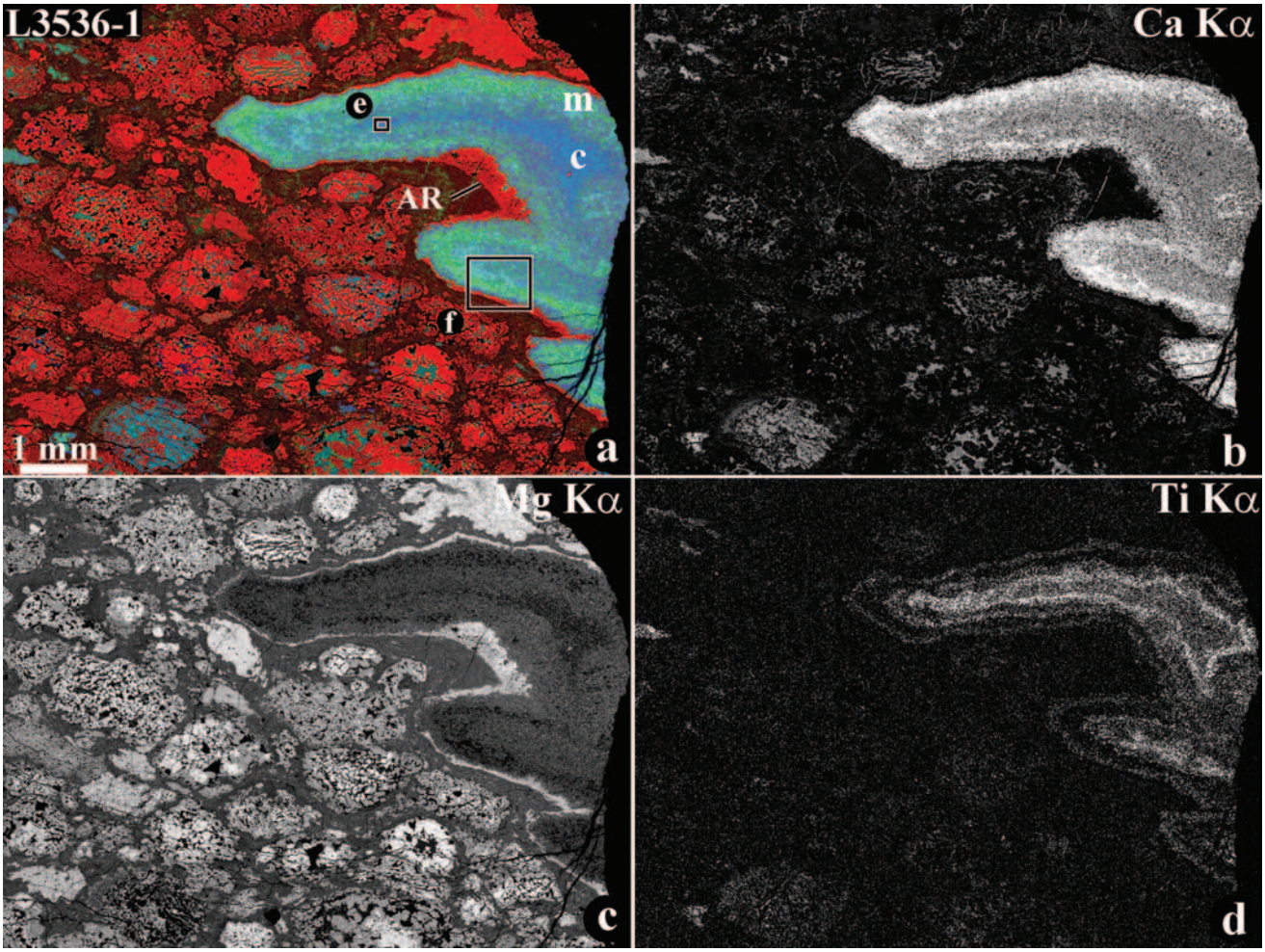

Fig. 4. Zoned, fine-grained, spinel-rich CAI L3536-1 from Leoville: a) combined X-ray elemental map (Mg = red, Ca = green, Al = blue); b, c, and d) individual X-ray element area maps for Ca (b), Mg (c), and Ti Kα (d); see text for details. The Ca-poor core consists of spinel ± perovskite, anorthite, and Al-diopside. The Ca-rich mantle is composed of Al-diopside, melilite, anorthite, and spinel. The CAI is surrounded by spinel and Al-diopside layers and a forsterite-rich accretionary rim (AR) that shows up clearly as a red surface layer in the combined X-ray map (a); fo = forsterite; the other abbreviations are as used previously.

grains, and each nodule is surrounded by a typical thick layer of anorthite and a thin wispy layer of Al-Ti-rich pyroxene (Fig. 5d). The mantle is composed of melilite that locally encloses spinel and is itself enclosed by Al-diopside; the melilite is replaced by anorthite (Fig. 5d).

Melilite-Poor Inclusions

Four of the CAIs we studied are depleted in melilite relative to those described so far. The first of these, Efremovka E51, has moderately complex zoning (Fig. 6). A large Ca-poor central region (Fig. 6b) consists of a Mg-rich inner core (Fig. 6c) and Mg-poor outer core (Fig. 6c), both of which display considerable complexity. The Ca-rich mantle of the CAI (Figs. 6a and 6b) is thin relative to the mantles of many of the inclusions discussed above. Once again, the shapes of all the layers, and their diffuse boundaries, are concentric with one another and mimic the outer edge of the CAI. The inner core consists of aggregates of subhedral spinel grains (some up to ~20 μm in size but most are smaller), each surrounded by a thin layer of Al-diopside; anorthite is very minor (Fig. 6e). Spinel grains in some of the aggregates show 120° triple junctions. The outer core differs primarily in having abundant anorthite and less abundant pyroxene (Fig. 6e). The outer core exhibits a gradation in properties across its own thickness, with spinel and Al-diopside decreasing in abundance outward and forsterite (just discernable as red dots in the composite X-ray area map in Fig. 6a and more easily seen as bright dots in the Mg Kα X-ray area map in Fig. 6c) simultaneously becoming abundant. The mantle is marked by a sharp increase in the abundance of pyroxene relative to the outer core (Figs. 6a and 6f). Toward the CAI edge, the thickness of the Al-diopside layers gradually increases so that the outer part of the CAI is quite pyroxene-rich. Melilite occurs only in the outermost ~100–200 μm portion of the mantle, where it partially encloses spinel. The melilite, in turn, is partially mantled by anorthite,

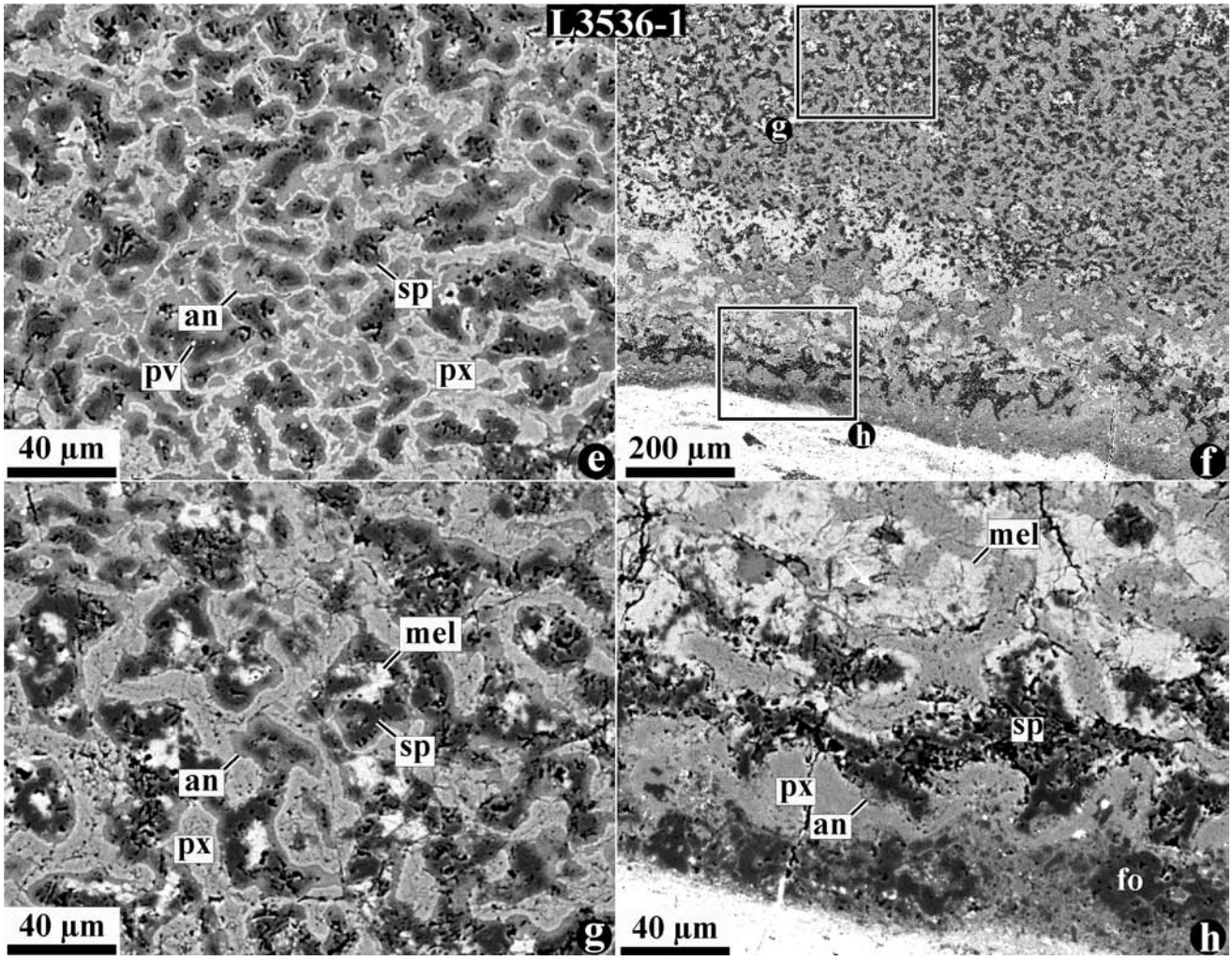

Fig. 4. *Continued.* Zoned, fine-grained, spinel-rich CAI L3536-1 from Leoville: e and f) BSE images of the regions outlined and labeled in (a); g and h) BSE images of the regions outlined and labeled in (f); see text for details. The Ca-poor core consists of spinel ± perovskite, anorthite, and Al-diopside. The Ca-rich mantle is composed of Al-diopside, melilite, anorthite, and spinel. The CAI is surrounded by spinel and Al-diopside layers and a forsterite-rich accretionary rim (AR) that shows up clearly as a red surface layer in the combined X-ray map (a); fo = forsterite; the other abbreviations are as used previously.

which occurs as thin selvages separating the melilite from the pyroxene (Fig. 6f).

Inclusion E14 has been studied previously (Ulyanov 1984; Boynton et al. 1986; Wark et al. 1986) and possesses a group II REE pattern (Boynton et al. 1986). It is simpler than E51, having a thick Ca-rich mantle enclosing a relatively small Ca-poor core (Figs. 7a–7c). Similar to E51, but unlike most of the other inclusions described above, the core of E14 contains very little anorthite associated with its irregularly shaped spinel nodules and surrounding thin layers of Al-diopside (Figs. 7d and 7e). Anorthite is much more abundant in the mantle, where it occurs as thin layers separating spinel grains from their enveloping Al-diopside layers (Figs. 7d and 7f). The anorthite is densely choked with micron-size spinel grains (Fig. 7g) and, in general, appears to replace spinel. Moving outward through the mantle, the abundance of spinel first decreases and then increases again, while the abundances of Al-diopside and anorthite progressively increase. Perovskite and melilite occur only in the outermost portion of the inclusion, the perovskite as tiny inclusions inside spinel and the melilite as partial mantles outside of spinel (Fig. 7g). The CAI is surrounded by a discontinuous and porous accretionary rim that is composed mostly of an aggregate of forsterite grains, tiny Al-diopside crystals, and Fe, Ni-metal.

Inclusion E101b is peculiar in having a smoothly elliptical shape (Fig. 8), in contrast to the very irregular CAIs described thus far. It contains no melilite, but in other aspects, it follows the familiar pattern of having a Ca-poor core (irregularly shaped spinel nodules surrounded by anorthite and Al-diopside) and a Ca-rich (pyroxene-rich and spinel-depleted) mantle (Fig. 8e). The CAI is surrounded by a prominent and densely crystalline forsterite-rich rim (Fig. 8f).

Leoville inclusion L3535-5 also contains no melilite (Fig. 9). The Ca-poor core of this irregularly shaped object

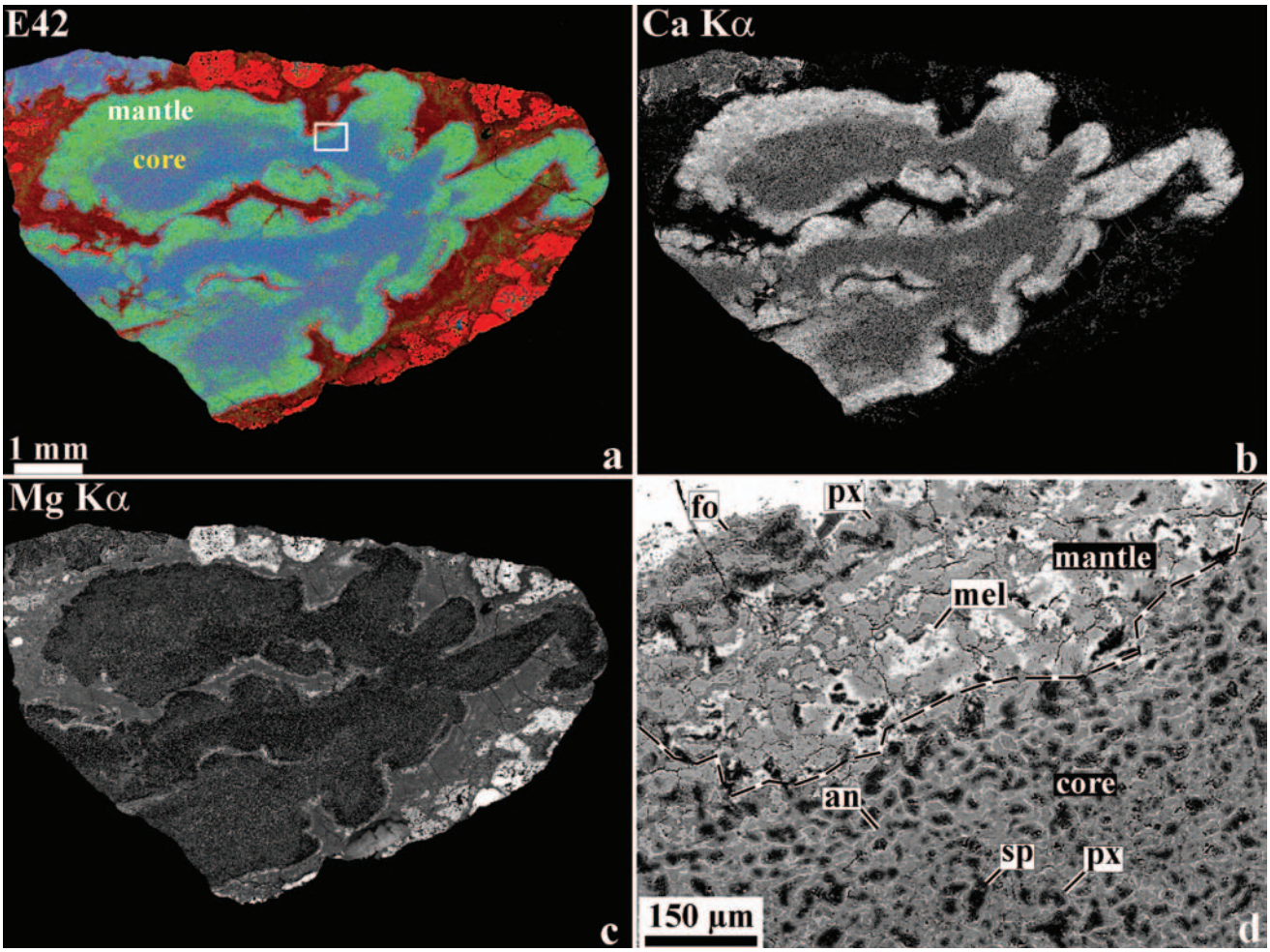

Fig. 5. Zoned, fine-grained, spinel-rich CAI E42 from Efremovka: a) combined X-ray elemental map; b and c) individual X-ray element area maps for Ca (b) and Mg Kα (c); d) BSE image of the region outlined and labeled in (a); see text for details. The Ca-poor core consists of spinel, anorthite, and minor Al-diopside. The Ca-rich mantle is made of Al-diopside, melilite, minor spinel, and anorthite. The CAI is surrounded by a thin forsterite-rich accretionary rim. The abbreviations are as used previously.

(Fig. 9b) is exceptionally fine-grained and contains abundant tiny spinel grains enveloped in a sea of anorthite and sparse, ragged Al-Ti-rich pyroxene grains (Fig. 9e). An unusual feature of L3535-5 is the occurrence of several large clumps of forsterite within the interior of the CAI (Figs. 9a and 9e). At the boundary between the core and mantle, anorthite is replaced by nepheline. The mantle itself is dominated by Al-diopside, with anorthite and spinel being less abundant than in the core. The CAI is surrounded by an accretionary rim made of coarse-grained forsterite, Fe, Ni-metal, and scattered refractory nodules composed of spinel, anorthite, and Al-diopside (Figs. 9a and 9f).

Compound Inclusion E49-A

Efremovka E49-a is a compound object composed of a zoned, fine-grained, spinel-rich inclusion and a coarse-grained, melilite-rich (type A) inclusion (Fig. 10). Its identity as a compound arises from trace element data that reveal the fine-grained portion to have a volatility-fractionated (group II) REE signature, while the type A portion has an unfractionated REE pattern (Huss et al. 2002). The fine-grained portion has a Ca-poor core and a Ca-rich mantle. The core consists of irregularly shaped spinel-perovskite nodules surrounded by the anorthite and Al-diopside layers (Fig. 10e). Toward the outer part of the core, the thickness of the Al-diopside layer increases (Fig. 10e). The mantle consists of irregularly shaped, compact regions of melilite ± spinel, each surrounded by a thick continuous layer of Al-diopside (Fig. 10f). The melilite is partially replaced by a fine-grained mixture of spinel and Al-diopside. The fine-grained inclusion is surrounded by the spinel and Al-diopside layers. The top-left (on Fig. 10) portion of E49-a is a coarse-grained, melilite-rich (type A) CAI. It consists of multiple melilite-spinel-perovskite nodules rimmed by Al-diopside (Figs. 10g and 10h). The melilite is replaced by a fine-grained mixture of Al-diopside and spinel; it contains abundant inclusions of perovskite and several massive spinel-melilite-perovskite ± hibonite nodules.

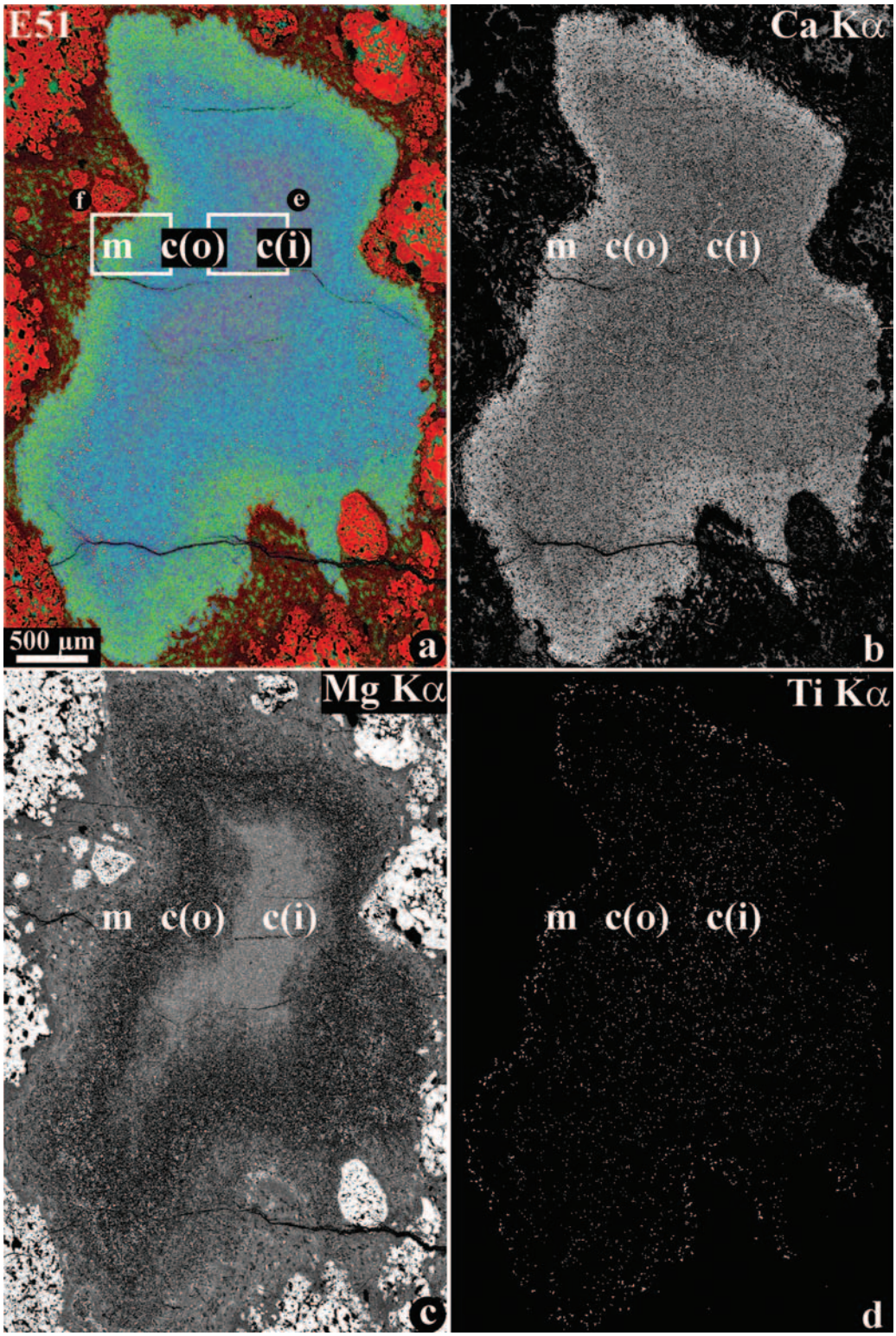

Fig. 6. Zoned, fine-grained, spinel-rich CAI E51 from Efremovka: a) combined X-ray elemental map (Mg = red, Ca = green, Al = blue); b, c, and d) individual X-ray element area maps for Ca (b), Mg (c), and Ti Kα (d); see text for details. The CAI has a Ca-poor core and a Ca-rich mantle (m). The core can be tentatively subdivided into a Mg-rich inner part (c[i]) and a Mg-poor outer part (c[o]). The inner part consists of spinel and Al-diopside; the outer part is made of spinel, coarse-grained Al-diopside, and abundant anorthite. The mantle consists of Al-diopside, spinel, anorthite, and minor melilite. Al-diopside in the outermost part of the mantle is enriched in Ti. The abbreviations are as used previously.

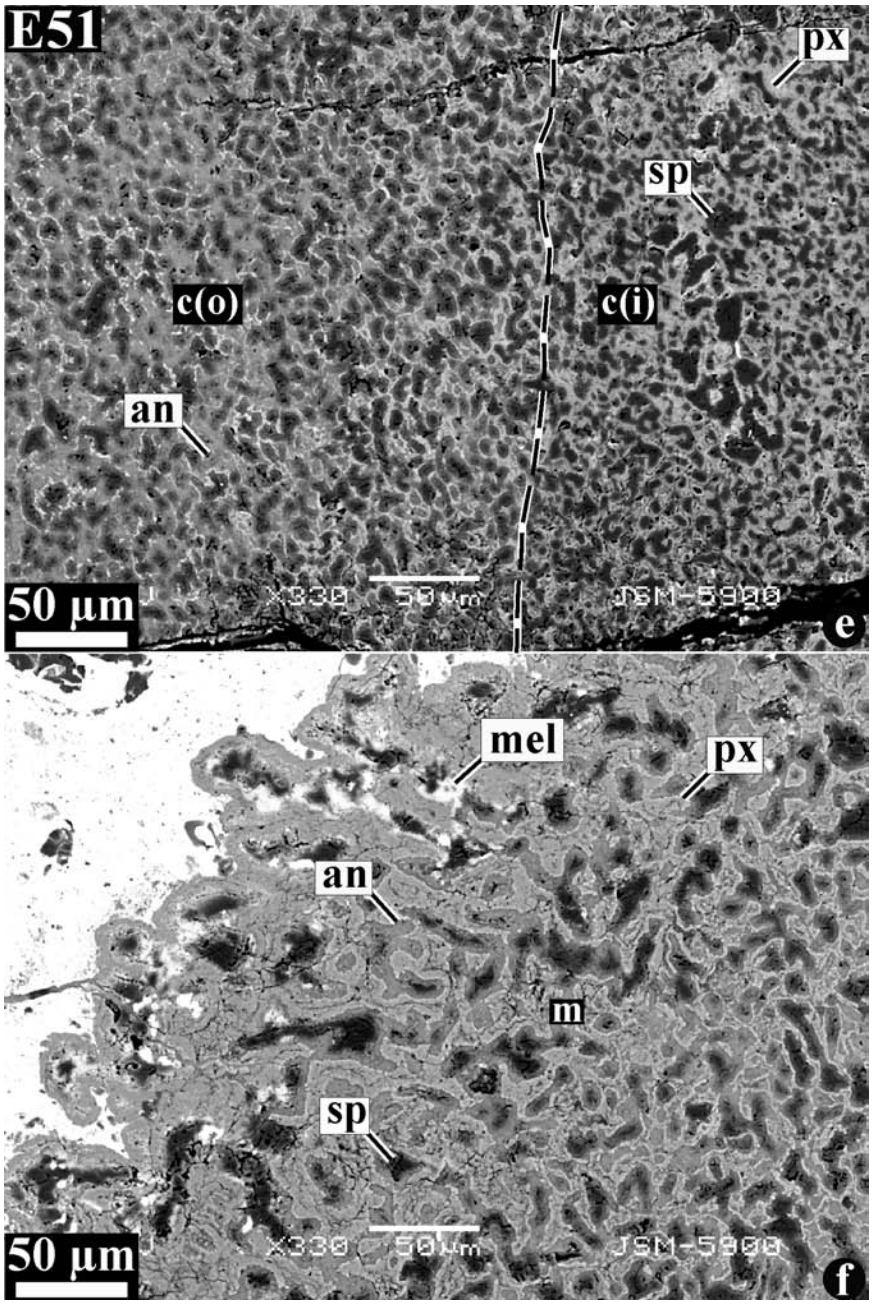

Fig. 6. *Continued.* Zoned, fine-grained, spinel-rich CAI E51 from Efremovka: e and f) BSE images of the regions outlined and labeled in (a); see text for details. The CAI has a Ca-poor core and a Ca-rich mantle (m). The core can be tentatively subdivided into a Mg-rich inner part (c[i]) and a Mg-poor outer part (c[o]). The inner part consists of spinel and Al-diopside; the outer part is made of spinel, coarse-grained Al-diopside, and abundant anorthite. The mantle consists of Al-diopside, spinel, anorthite, and minor melilite. Al-diopside in the outermost part of the mantle is enriched in Ti. The abbreviations are as used previously.

Mineral Chemistry

There are no compositional differences between minerals in the Efremovka versus Leoville CAIs; below, we discuss them together.

Spinel in the interiors of these Efremovka and Leoville fine-grained inclusions is uniformly FeO-poor (mean ~0.4 wt%) and has low concentrations of MnO (<0.07 wt%), TiO_2 (0.09–0.45 wt%), and Cr_2O_3 (0.07–1.3 wt%) (Table 2). Spinel in the CAI rims is enriched in FeO (up to 7.7 wt%). In the compound CAI E49-a, spinel in the core of the main part of the inclusion is enriched in Cr_2O_3 (1.2 wt%) relative both to spinel in its mantle (0.21 wt%) and to the "attached" exterior type A (melilite-rich) material (0.16 wt%).

Even the most FeO-rich compositions noted above are

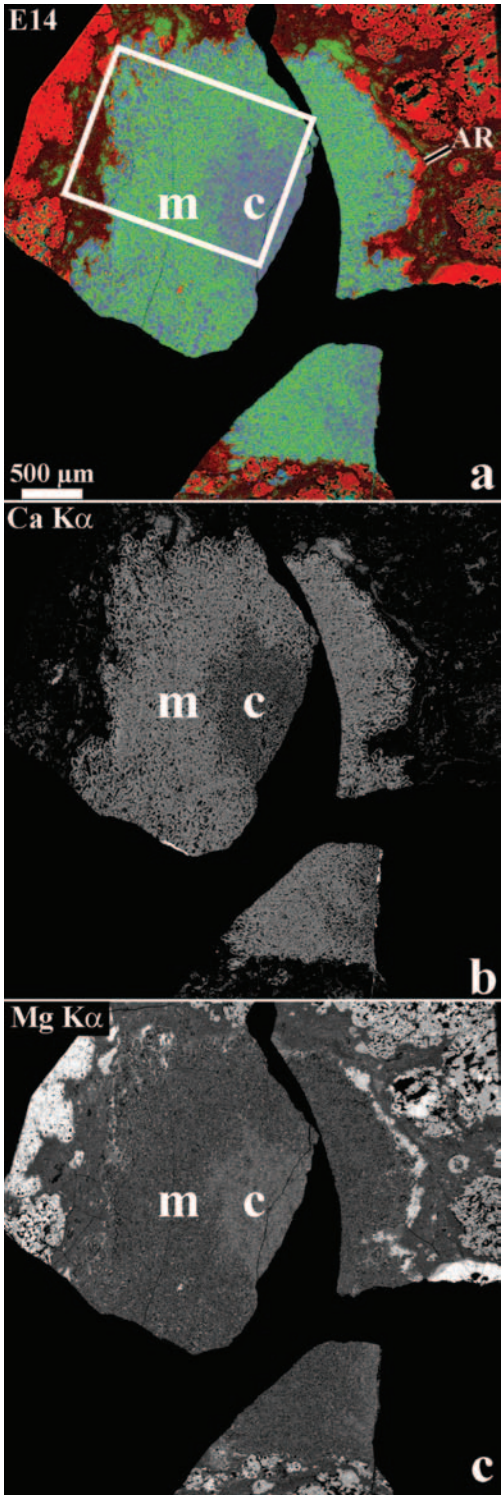

Fig. 7. Zoned, fine-grained, spinel-rich inclusion E14 from Efremovka: a) combined X-ray elemental map; b and c) individual X-ray element area maps for Ca (b) and Mg (c); see text for details. The Ca-poor core consists of spinel surrounded by Al-diopside. The Ca-rich mantle is composed of spinel surrounded by anorthite and Al-diopside. The CAI is surrounded by a discontinuous forsterite-rich accretionary rim (AR). The abbreviations are as used previously.

much lower in FeO than the compositions of spinel in fine-grained inclusions observed in Allende and other oxidized subgroup CVs (e.g., McGuire and Hashimoto 1989).

Hibonites span a wide range of compositions in both TiO_2 (0.5–5.3 wt%) and MgO (0.37–3.0 wt%); the concentrations of other elements are generally low (Table 3). Hibonite in the melilite-rich type A portion of the compound inclusion E49-a has substantially higher concentrations of TiO_2 (7.7 wt%) and MgO (4.3 wt%). On a diagram plotting total atomic divalent + quadrivalent versus trivalent cations (Fig. 11), compositions of hibonite in Leoville and Efremovka fine-grained inclusions plot very close to a 1:1 correlation line, implying the coupled substitution:

$$R^{4+} + R^{2+} = 2\ R^{3+}$$

Pyroxene chemistry varies significantly and systematically, on a large scale from the interiors to the exteriors of the CAIs and on a microscale across individual layers (Table 4; Fig. 12).

Pyroxene in the inclusion mantles tends to be Al-rich diopside with <8–10 wt% Al_2O_3 and <1–2 wt% TiO_2. Pyroxene in the inclusion cores exists as tiny grains that are difficult to analyze with high precision, but persistent efforts in L3536-1 yielded analyses showing much greater enrichment in Al_2O_3 (up to ~19 wt%) and TiO_2 (up to 9 wt%) (Fig. 12). Close examination of backscattered electron images shows that the interior pyroxenes in all of the zoned CAIs have brighter electron albedos (owing to a higher mean atomic number) than do those in the mantles,

Table 3. Representative microprobe analyses of hibonite in fine-grained, spinel-rich CAIs from Efremovka and Leoville.

Ox\no	E103a		E49-a[a]	L3535-5f	
SiO_2	0.10	0.28	0.46	0.74	0.19
TiO_2	0.50	5.1	7.7	2.0	5.3
Al_2O_3	91.1	83.8	80.4	89.2	85.1
Cr_2O_3	<0.07	<0.07	<0.07	<0.07	<0.07
FeO	<0.08	<0.08	<0.08	0.41	<0.08
MnO	<0.07	<0.07	<0.07	<0.07	<0.07
MgO	0.37	2.6	4.3	1.1	3.0
CaO	8.6	8.4	8.3	8.4	8.1
Na_2O	<0.06	<0.06	<0.06	<0.06	<0.06
Total	100.6	100.2	101.1	101.9	101.8
Structural formulae based on 19 O					
Si	0.011	0.032	0.051	0.082	0.021
Ti	0.041	0.431	0.645	0.165	0.438
Al	11.874	11.079	10.592	11.528	11.075
Cr	–	–	–	–	–
Fe	–	–	–	0.037	–
Mn	–	–	–	–	–
Mg	0.061	0.432	0.721	0.180	0.501
Ca	1.015	1.012	0.988	0.991	0.960
Na	–	–	–	–	–
Total	13.003	12.985	12.997	12.983	12.995

[a]Coarse-grained, melilite-rich portion.

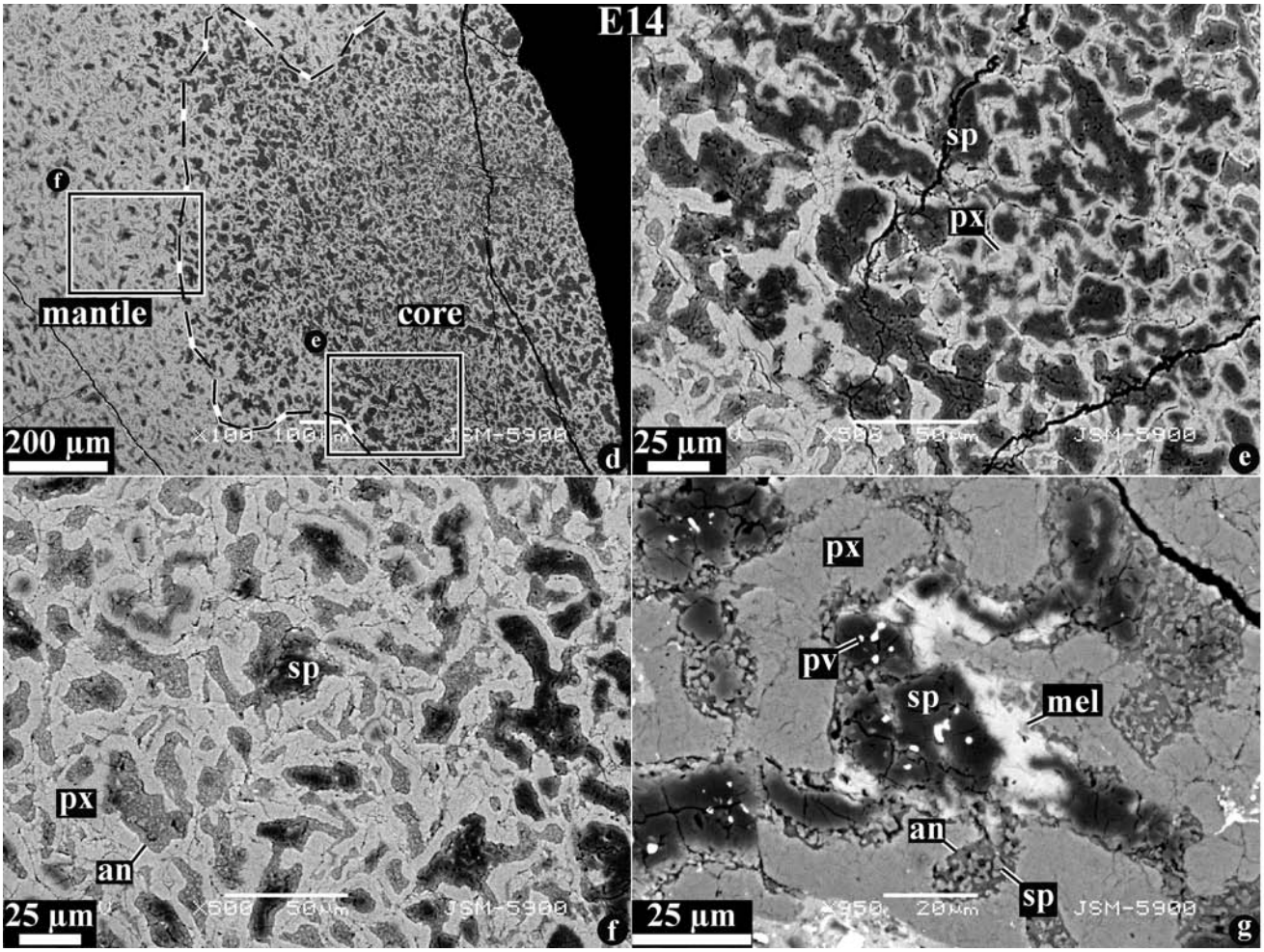

Fig. 7. *Continued.* Zoned, fine-grained, spinel-rich inclusion E14 from Efremovka: d) BSE image of the region outlined in (a); e and f) detailed BSE images of the regions outlined in (d); g) detailed BSE image of part of the CAI mantle, showing melilite surrounding spinel (with perovskite inclusions) and with a dense intergrowth of anorthite + spinel replacing melilite; see text for details. The Ca-poor core consists of spinel surrounded by Al-diopside. The Ca-rich mantle is composed of spinel surrounded by anorthite and Al-diopside. The CAI is surrounded by a discontinuous forsterite-rich accretionary rim (AR). The abbreviations are as used previously.

suggesting that this compositional difference between core versus mantle pyroxene is general and not restricted to only L3536-1.

Within individual pyroxene layers, the abundance of Al_2O_3 increases toward anorthite and spinel.

Melilite in all of the inclusions we analyzed is aluminum-rich: the total range of compositions is $Åk_{0–35}$, with 85% of the analyses having Åk <20 and 58% of the analyses having Åk <10 (Table 5; Fig. 13). Individual melilite crystals are too small to measure internal compositional zoning. Some melilite analyses show detectable concentrations (>0.06 wt%) of Na_2O, which shows a slight positive correlation with åkermanite content.

Plagioclase was analyzed only in reconnaissance fashion, in part because the very small grains commonly have numerous tiny inclusions of pyroxene and/or spinel that make it difficult to obtain clean high-quality analyses. Our limited data show that the plagioclase is nearly pure anorthite ($CaAl_2Si_2O_8$) in composition, with most analyses having less than 0.1 wt% Na_2O.

Olivine, mostly analyzed in accretionary rims around fine-grained inclusions, is forsterite ($Fa_{<3.7}$) with low or undetectable contents of TiO_2, Al_2O_3, Cr_2O_3, CaO, and MnO (Table 6).

Perovskite in most of these CAIs is too fine-grained to analyze quantitatively by electron microprobe, and we made cursory analyses to confirm its identity only.

Bulk Chemistry

Bulk compositions of fine-grained, spinel-rich inclusions (including separate core and mantle analyses of compositionally zoned inclusions) are listed in Table 7 and plotted in Figs. 14–16. Most bulk inclusions, including both their cores and mantles, show significant fractionation of Ca from Al (Fig. 14). All unzoned, fine-grained CAIs have

Table 4. Representative microprobe analyses of pyroxene in fine-grained CAIs from Efremovka and Leoville.

							E42				E49-a	
Ox\no	E101b-1	L3535-5f		L3536-1			core		mantle		core	mantle
SiO_2	56.3	54.9	53.0	52.3	50.0	41.4	54.7	47.8	53.7	48.2	53.8	54.5
TiO_2	<0.05	0.05	0.08	0.34	2.6	7.1	0.08	3.2	0.17	0.93	0.72	0.11
Al_2O_3	1.0	1.5	5.0	6.1	7.0	16.4	1.1	8.7	2.8	11.4	2.9	2.1
Cr_2O_3	0.07	<0.07	0.08	<0.07	<0.07	0.15	0.18	0.15	0.08	0.13	0.08	<0.07
FeO	0.48	2.0	1.6	0.51	<0.08	<0.08	<0.08	<0.08	0.08	<0.08	0.09	0.12
MnO	<0.07	<0.07	<0.07	<0.07	<0.07	<0.07	<0.07	<0.07	0.07	<0.07	<0.07	<0.07
MgO	19.2	17.7	16.2	16.4	16.1	11.2	18.9	14.9	18.2	14.7	17.9	18.1
CaO	24.9	24.3	23.7	25.1	25.0	25.1	24.2	24.2	25.4	25.6	24.5	25.3
Na_2O	<0.06	<0.06	<0.06	<0.06	<0.06	<0.06	<0.06	<0.06	<0.06	<0.06	<0.06	<0.06
Total	102.0	100.4	99.8	100.8	100.8	101.5	99.2	99.1	100.6	101.0	100.0	100.3
Structural formulae based on 6 O												
Si	1.984	1.977	1.917	1.872	1.794	1.494	1.980	1.746	1.926	1.728	1.932	1.954
Ti	0.000	0.001	0.002	0.009	0.070	0.194	0.002	0.088	0.005	0.025	0.020	0.003
Al	0.043	0.062	0.213	0.255	0.297	0.698	0.046	0.376	0.120	0.480	0.123	0.090
Cr	0.002	–	0.002	–	–	0.004	0.005	0.004	0.002	0.004	0.002	–
Fe	0.014	0.061	0.048	0.015	0.001	0.000	0.001	0.002	0.002	0.000	0.003	0.004
Mn	–	–	–	–	–	–	–	–	0.002	–	–	–
Mg	1.007	0.950	0.870	0.873	0.861	0.603	1.020	0.811	0.974	0.785	0.961	0.970
Ca	0.939	0.937	0.919	0.963	0.961	0.968	0.939	0.948	0.976	0.983	0.943	0.974
Na	–	–	–	–	–	–	–	–	–	–	–	–
Total	3.996	3.991	3.975	3.990	3.988	3.962	3.993	3.977	4.009	4.006	3.986	3.995

	E51				E101b						
Ox\no	core	rim	E14		core		mantle		L3535-5		
SiO_2	49.17	53.8768	55.1	52.8	53.4	47.6	54.0	47.3	55.2	48.7	55.9
TiO_2	0.08	0.06	0.05	0.89	0.11	0.76	0.12	2.5	0.13	0.83	0.11
Al_2O_3	11.5	2.7	0.91	2.6	3.7	12.1	1.5	10.1	1.8	10.6	0.50
Cr_2O_3	0.0799	<0.07	0.07	0.08	0.07	0.12	<0.07	0.08	<0.07	<0.07	<0.07
FeO	<0.08	0.1202	0.43	0.08	0.12	0.22	0.76	0.71	0.34	1.1	0.09
MnO	<0.07	<0.07	<0.07	<0.07	<0.07	<0.07	<0.07	0.07	<0.07	<0.07	<0.07
MgO	15.5114	18.3393	19.2	18.4	17.2	14.5	18.0	14.7	18.7	14.1	19.2
CaO	24.1	24.8	24.6	24.3	25.4	24.3	24.3	24.5	24.8	23.9	24.6
Na_2O	<0.06	<0.06	<0.06	<0.06	<0.06	<0.06	<0.06	<0.06	<0.06	<0.06	<0.06
Total	100.4	99.9	100.4	99.3	100.0	99.7	98.7	100.0	101.1	99.3	100.5
Structural formulae based on 6 O											
Si	1.757	1.938	1.975	1.917	1.924	1.723	1.971	1.719	1.965	1.770	1.996
Ti	0.002	0.002	0.001	0.024	0.003	0.021	0.003	0.069	0.003	0.023	0.003
Al	0.486	0.116	0.039	0.113	0.156	0.516	0.065	0.430	0.077	0.455	0.021
Cr	0.002	–	0.002	0.002	0.002	0.003	–	0.002	–	–	–
Fe	–	0.004	0.013	0.003	0.004	0.007	0.023	0.022	0.010	0.034	0.003
Mn	–	–	–	–	–	–	–	0.002	–	–	–
Mg	0.826	0.984	1.028	0.996	0.925	0.783	0.979	0.797	0.991	0.763	1.023
Ca	0.921	0.956	0.945	0.946	0.979	0.944	0.950	0.954	0.946	0.932	0.942
Na	–	–	–	–	–	–	–	–	–	–	–
Total	3.995	3.999	4.003	4.002	3.994	3.997	3.993	3.996	3.994	3.979	3.989

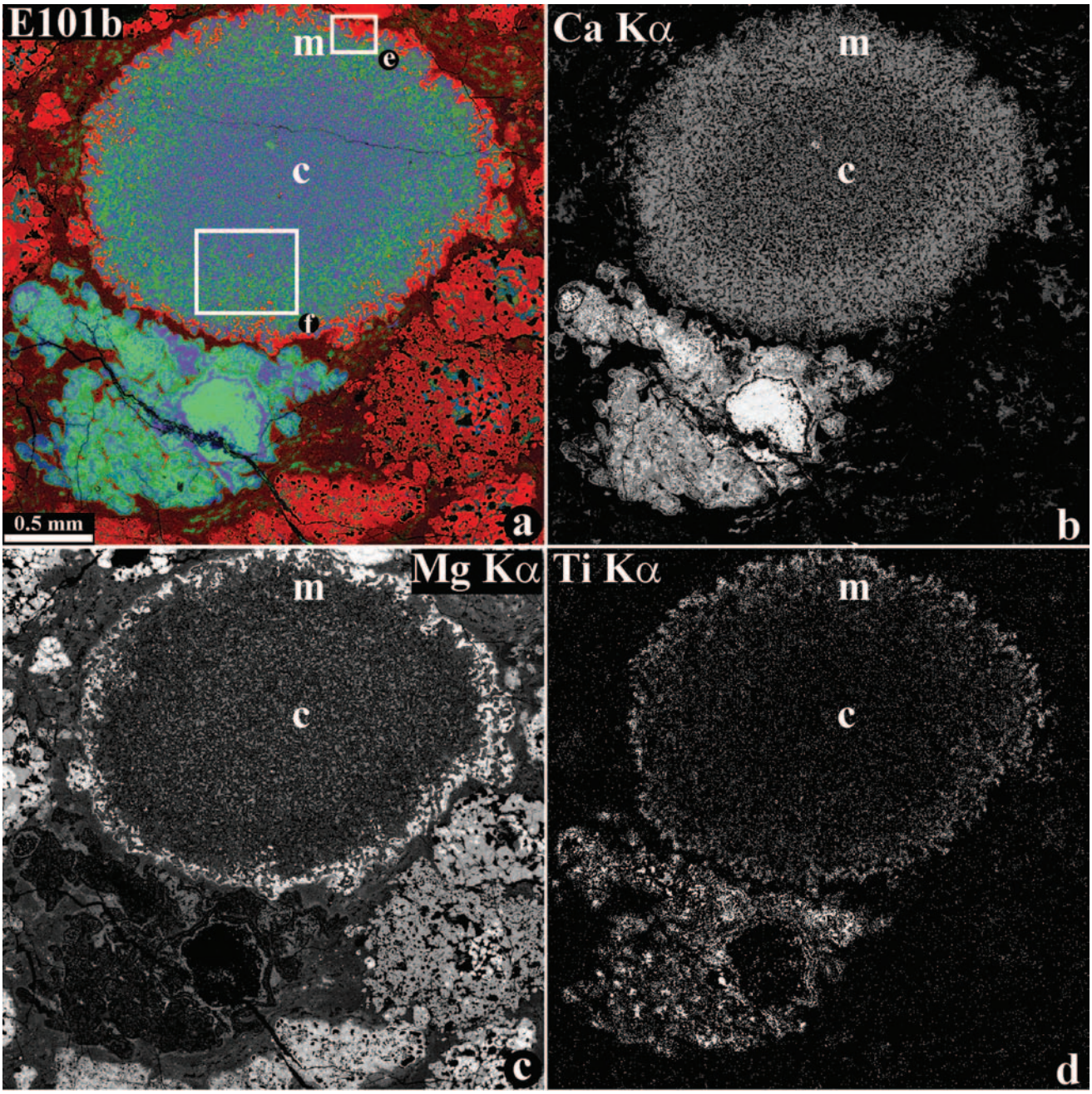

Fig. 8. Zoned, fine-grained, spinel-rich inclusion E101b from Efremovka: a) combined X-ray elemental map; b, c, and d) individual X-ray element area maps for Ca (b), Mg (c), and Ti Kα (d); see text for details. The Ca-poor pore core and Ca-rich mantle of the CAI consist of spinel, Al-diopside, and anorthite. The mantle has coarser-grained Al-diopside and less spinel than the core. The CAI is surrounded by a forsterite-rich layer that is well-shown (red) in (a). The abbreviations are as used previously.

subchondritic Ca/Al ratios (Fig. 14a). Some zoned, fine-grained CAIs, melilite-rich (e.g., E103a) and melilite-poor (e.g., E51), have subchondritic Ca/Al ratios in both the core and the mantle (Figs. 14b and 14d). Others (e.g., E42, E49-a) have mantle zones with superchondritic Ca/Al ratios and cores with complementary subchondritic Ca/Al ratios (Fig. 14c). However, since the volumes of the mantles are significantly smaller than those of the cores, the bulk compositions of nearly all of the CAIs have subchondritic Ca/Al rich ratios.

Most of the fine-grained inclusions are depleted in Ti relative to Ca and Al; this depletion is generally smaller in inclusion mantles than inclusion cores (Figs. 14b–14d). Most inclusions are also enriched in Si relative to Mg, in both cores and mantles. The cores of the inclusions E49-a, E101b, and E103a are enriched in Cr relative to their mantles. These

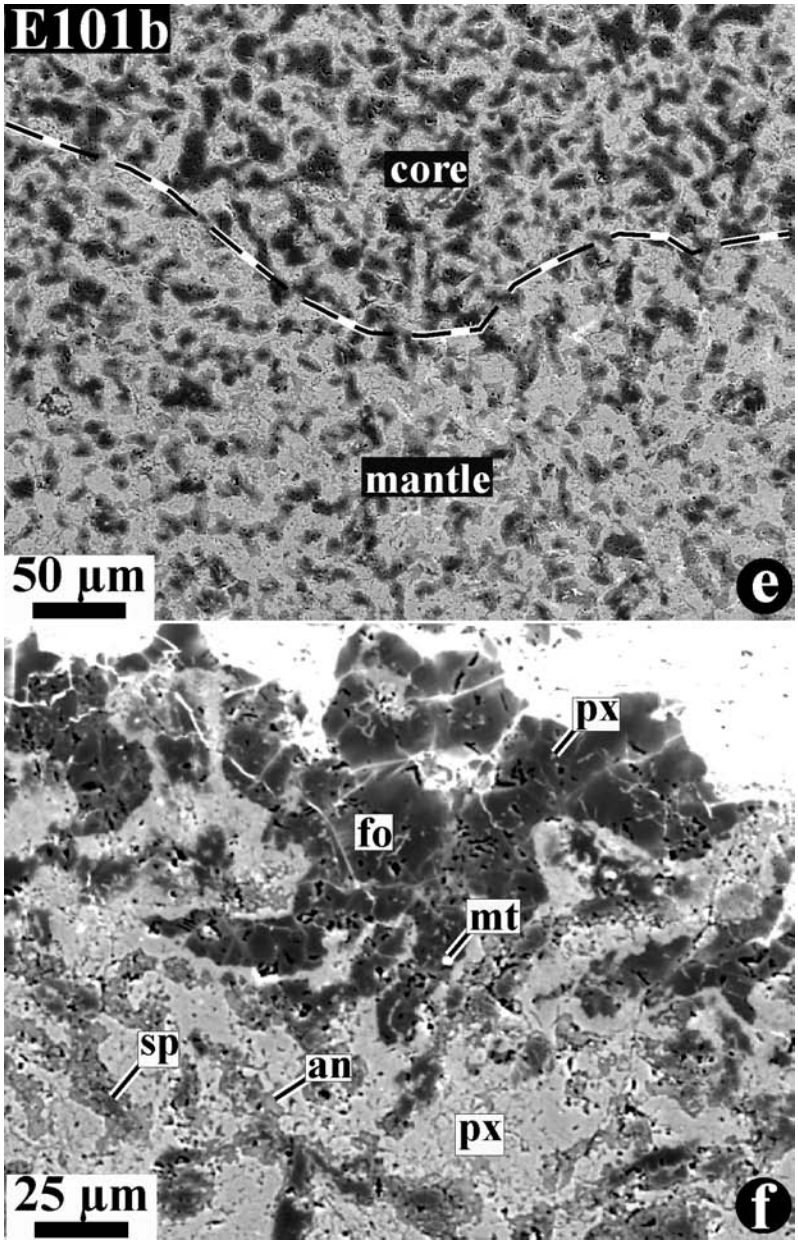

Fig. 8. *Continued.* Zoned, fine-grained, spinel-rich inclusion E101b from Efremovka: e and f) BSE images of the regions outlined and labeled in (a); see text for details. The Ca-poor pore core and Ca-rich mantle of the CAI consist of spinel, Al-diopside, and anorthite. The mantle has coarser-grained Al-diopside and less spinel than the core. The CAI is surrounded by a forsterite-rich layer that is well-shown (red) in (a). The abbreviations are as used previously.

fractionation patterns within individual inclusions are the reverse of what might be expected from condensation considerations, i.e., the inclusions are more refractory on their exteriors than in their interiors. This inverse chemical zoning parallels the inverse mineralogical zonation in the same CAIs: the mantles contain abundant refractory melilite, while the cores are melilite-free and contain abundant less-refractory anorthite.

A different way of looking at these relationships is shown in Figs. 15 and 16, where bulk compositions of fine-grained inclusions are projected (from spinel) onto the ternary diagram Ca_2SiO_4-Mg_2SiO_4-Al_2O_3. The core-mantle trends for the fine-grained inclusions are shown in Fig. 15, relative to the spinel-saturated liquidus surface and to the trend defined by total condensed solids during equilibrium condensation of a solar gas (Yoneda and Grossman 1995). As is the case for other CAI varieties, the trend defined by the bulk compositions of these fine-grained, spinel-rich inclusions shows no relation to liquidus phase boundaries. Thus, the bulk compositions are not the result of igneous fractionation processes. The trend does, however, bear similarity to the trend predicted by equilibrium condensation calculations for a hot gas of solar

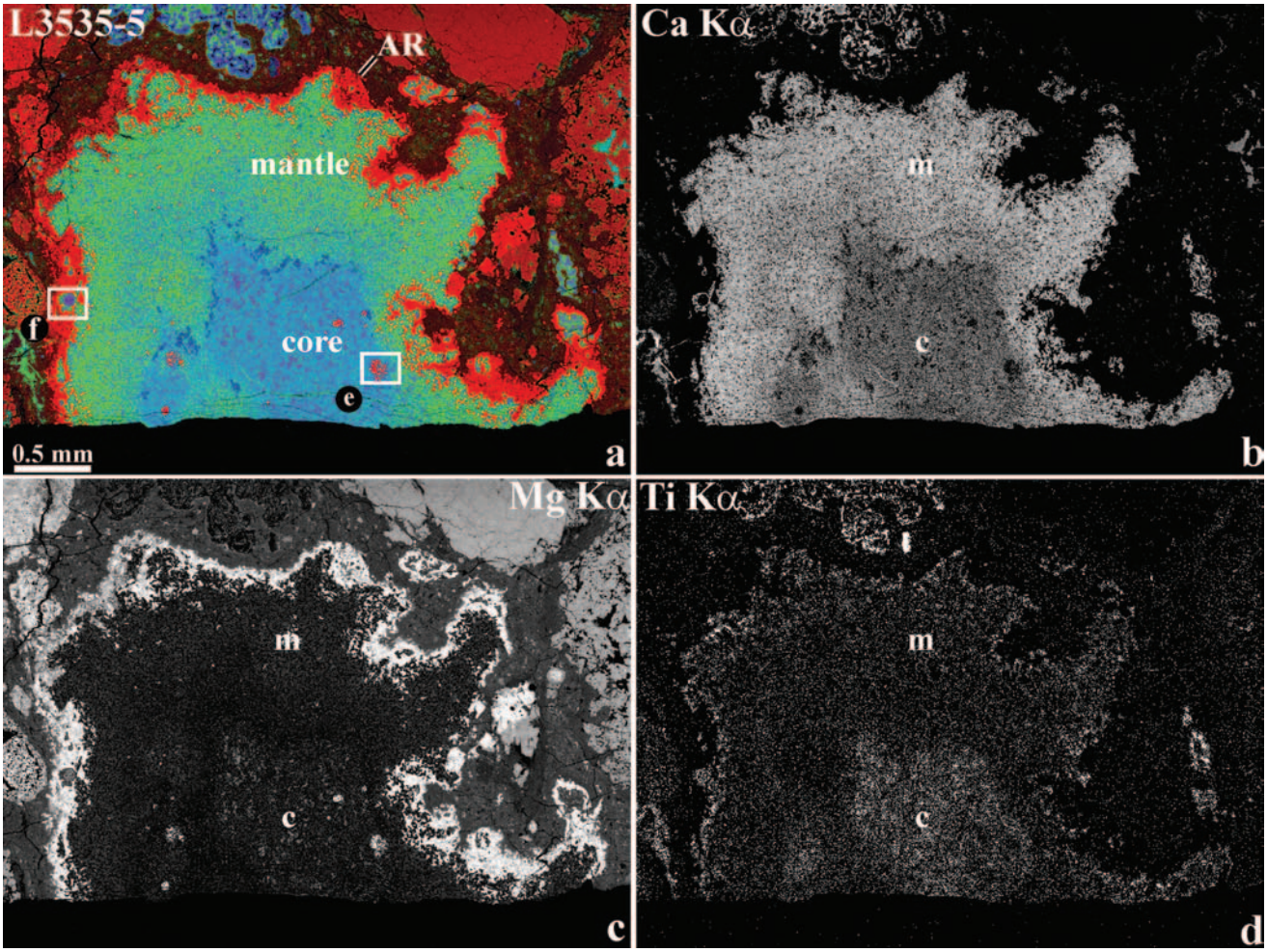

Fig. 9. Zoned, fine-grained, spinel-rich inclusion L3535-5 from Leoville: a) combined X-ray elemental map (Mg = red, Ca = green, Al = blue); b, c, and d) individual X-ray element area maps for Ca (b), Mg (c), and Ti (d); see text for details. The CAI has a diffuse core-mantle structure and is surrounded by a thick forsterite-rich accretionary rim (AR) that is clearly shown in (a). The Ca-poor core is exceptionally fine-grained and contains abundant tiny spinel grains surrounded by anorthite and sparse, ragged Al-Ti-rich pyroxene grains. The core also contains several forsterite regions and secondary nepheline. The Ca-rich mantle is dominated by Al-diopside, with anorthite and spinel being less abundant than in the core. The CAI is surrounded by an accretionary rim made of coarse-grained forsterite, Fe, Ni-metal, and scattered refractory nodules composed of spinel, anorthite, and Al-diopside; mt = metal. The other abbreviations are as used previously.

composition. For melilite-bearing zoned inclusions, the tie-lines joining core and mantle bulk compositions approximately parallel (but are offset from) the equilibrium condensation trend. However, the presumably first-formed cores actually plot in the down-temperature direction relative to the mantles; in other words, the core-mantle compositional trend is precisely opposite to that expected from the equilibrium condensation path. The core-mantle tie-lines of melilite-free, fine-grained inclusions parallel the anorthite-diopside join, but again, the anorthite-rich cores actually lie in the down-temperature direction because equilibrium condensation calculations predict anorthite to condense at a substantially lower temperature than pyroxene.

Figure 16 compares the total bulk compositions of fine-grained inclusions with those of types A, B, and C CAIs and aluminum-rich chondrules. Most of the fine-grained inclusions plot within the anorthite (+ spinel + liquid) primary phase volume; melts of such compositions will have anorthite or spinel as the first crystallizing phase. These compositions are distinctly more anorthite- and pyroxene-normative than those of either types A or B CAIs but overlap to a large degree with those of type C inclusions. The fine-grained CAIs are more melilite-normative than most Al-rich chondrules.

DISCUSSION

The Pristine Nature of Fine-Grained Inclusions in Efremovka and Leoville

The prototypical fine-grained, spinel-rich inclusions in Allende (CV_{ox}) contain abundant alkali-rich phases (nepheline and sodalite), iron-rich phases (hedenbergite, andradite, and

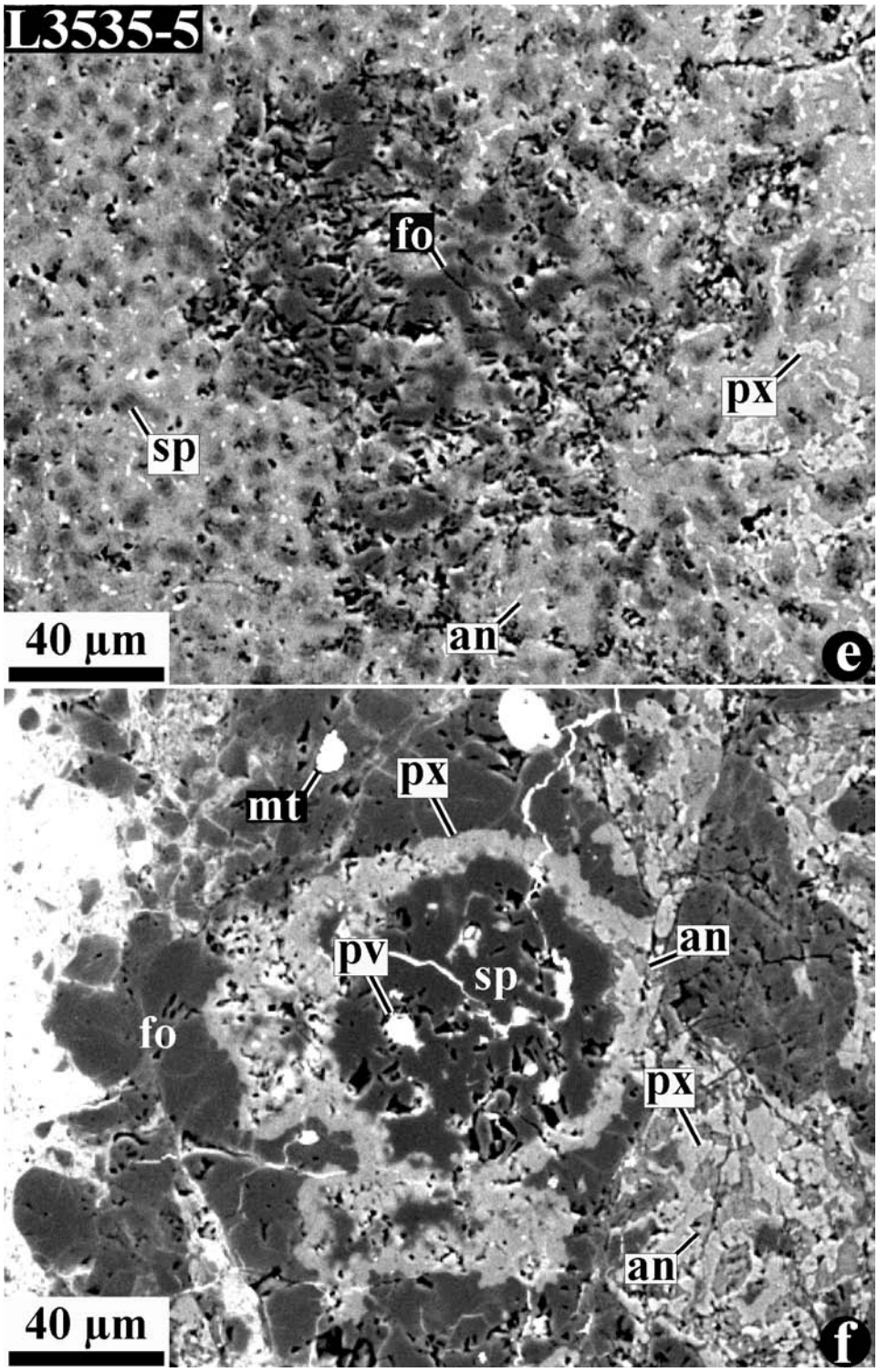

Fig. 9. *Continued.* Zoned, fine-grained, spinel-rich inclusion L3535-5 from Leoville: e and f) BSE images of regions outlined and labeled in (a); see text for details. The CAI has a diffuse core-mantle structure and is surrounded by a thick forsterite-rich accretionary rim (AR) that is clearly shown in (a). The Ca-poor core is exceptionally fine-grained, and contains abundant tiny spinel grains surrounded by anorthite and sparse, ragged Al-Ti-rich pyroxene grains. The core also contains several forsterite regions and secondary nepheline. The Ca-rich mantle is dominated by Al-diopside, with anorthite and spinel being less abundant than in the core. The CAI is surrounded by an accretionary rim made of coarse-grained forsterite, Fe, Ni-metal, and scattered refractory nodules composed of spinel, anorthite, and Al-diopside; mt = metal. The other abbreviations are as used previously.

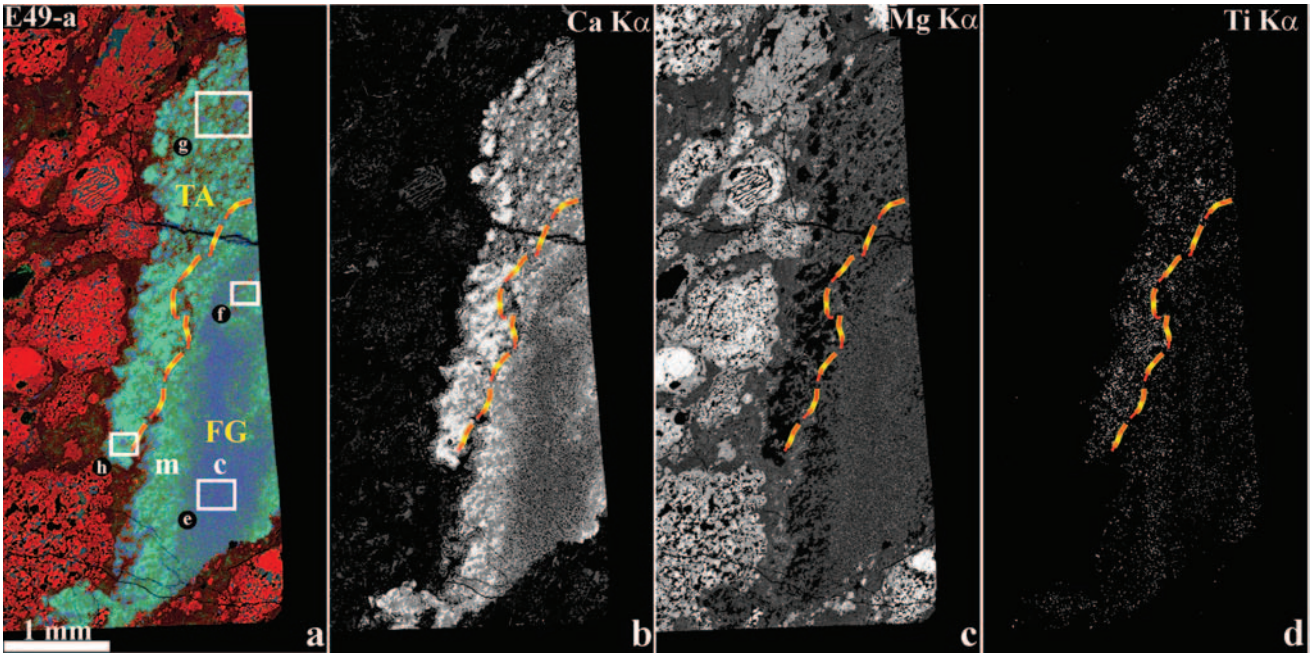

Fig. 10. The compound Efremovka CAI E49-a: a) combined X-ray elemental map (Mg = red, Ca = green, Al = blue); b, c, and d) individual X-ray element area maps for Ca (b), Mg (c), and Ti Kα (d); see text for details. The dominant portion of the CAI is a zoned, fine-grained, spinel-rich inclusion (FG); the upper left region (on a–d) is a coarse-grained, melilite-rich (type A, TA) inclusion. The boundary between these lithologies is indicated by a dashed line. The fine-grained CAI has a well-defined core-mantle structure. The Ca-poor core consists of irregularly shaped spinel-perovskite bodies, each surrounded by an anorthite layer and a thin layer of Al-diopside. The abundance and grain size of pyroxene increase, while the abundances of spinel and anorthite decrease, toward the CAI mantle. The Ca-rich mantle is composed of irregularly shaped melilite regions surrounded by coarse-grained Al-diopside. Melilite is replaced by a fine-grained mixture of Al-diopside and spinel. The type A part of the CAI consists of multiple melilite bodies, full of enclosed spinel and perovskite grains and rimmed by Al-diopside. Also present in this portion of the CAI are several large spinel-perovskite-melilite ± hibonite nodules (h). Melilite is corroded by a fine-grained mixture of spinel and Al-diopside.

ferrous olivine), grossular, and wollastonite. Detailed textural observations (e.g., McGuire and Hashimoto 1989) indicate that the alkali-bearing phases are replacing earlier-formed phases such as anorthite, melilite, and spinel and that the iron-bearing silicates fill in interstitially between other phases. Thus, the inclusions in Allende (and other oxidized subgroup CVs) are very complex and have experienced multi-stage histories. In general, calcium-aluminum-rich inclusions in the reduced CV chondrite Vigarano show less secondary mineralization than those in Allende and other oxidized CV chondrites, but even in Vigarano, the fine-grained, spinel-rich inclusions commonly contain alkali-bearing and iron-bearing secondary minerals. In contrast, the fine-grained, spinel-rich inclusions in the reduced CV chondrites Efremovka and Leoville are mostly lacking in hedenbergite, andradite, grossular, wollastonite, and ferrous olivine; only some spinel in the outermost portions of these CAIs show slight enrichment in oxidized iron. Alkali-rich phases are present but insignificant in amount, and are largely concentrated in the outer portions of these inclusions. Although by no means simple, the Leoville and Efremovka CAIs appear to record an earlier stage in the history of fine-grained, spinel-rich CAIs, predating the introduction of oxidized iron or significant alkalies. Therefore, it is significant that most fine-grained inclusions in Efremovka and Leoville show overall structural zonation in the distribution of minerals. This zoning must be a primary nebular signature, not a result of secondary alteration. The properties of these CAIs, thus, support earlier inferences (Hashimoto and Grossman 1985; McGuire and Hashimoto 1989), based on the observed mineral distributions in Allende inclusions, that the progenitors of the latter objects must have possessed a primary structural zonation. Likely, the Leoville and Efremovka CAIs are those progenitors. As discussed below, however, the actual nature of their primary zonation is not what was inferred from the earlier studies of the Allende fine-grained inclusions.

The existing mineralogic differences between fine-grained, spinel-rich inclusions in Allende versus those in Efremovka and Leoville are not simply a function of oxidized versus reduced CV subtype. Vigarano, for example, belongs to the reduced CV subtype, yet its fine-grained, spinel-rich inclusions contain iron-rich and alkali-rich phases like their counterparts in Allende. What sets the Efremovka and Leoville meteorites apart from the other CVs is their high degree of parent body compaction and deformation (MacPherson and Krot 2002). Chondrules, for example, are all deformed into ellipsoids. And, unlike Allende and Vigarano, which are both friable and can easily be sampled using simple

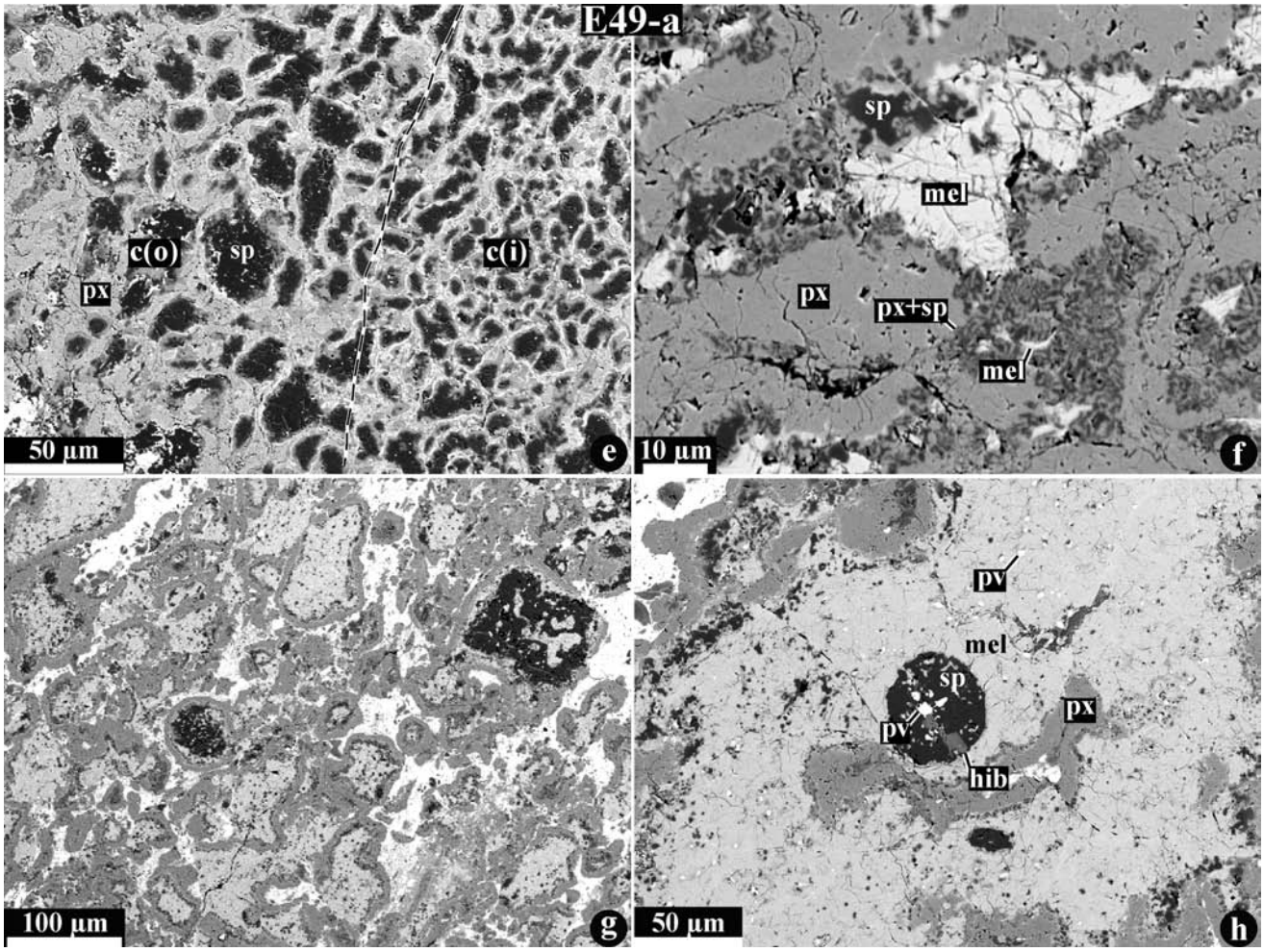

Fig. 10. *Continued.* The compound Efremovka CAI E49-a: e–h) BSE images of regions outlined and labeled in (a); see text for details. The dominant portion of the CAI is a zoned, fine-grained, spinel-rich inclusion (FG); the upper left region (on a–d) is a coarse-grained, melilite-rich (type A, TA) inclusion. The boundary between these lithologies is indicated by a dashed line. The fine-grained CAI has a well-defined core-mantle structure. The Ca-poor core consists of irregularly shaped spinel-perovskite bodies, each surrounded by an anorthite layer and a thin layer of Al-diopside. The abundance and grain size of pyroxene increase, while the abundances of spinel and anorthite decrease, toward the CAI mantle. The Ca-rich mantle is composed of irregularly shaped melilite regions surrounded by coarse-grained Al-diopside. Melilite is replaced by a fine-grained mixture of Al-diopside and spinel. The type A part of the CAI consists of multiple melilite bodies, full of enclosed spinel and perovskite grains and rimmed by Al-diopside. Also present in this portion of the CAI are several large spinel-perovskite-melilite ± hibonite nodules (h). Melilite is corroded by a fine-grained mixture of spinel and Al-diopside.

dental tools, Efremovka and Leoville are hard and tenacious rocks that can only be sampled by breaking or cutting. MacPherson and Krot (2002) interpreted the great rarity of andradite and hedenbergite in Leoville and Efremovka to be due to greatly reduced porosity arising from the parent body compaction. The compaction was likely caused by impacts (both meteorites exhibit strong foliations, and both are shock stage S3) and, therefore, the reduced porosity affected fluid flow on the parent body. Unlike Allende and Vigarano, andradite and hedenbergite were largely prevented from forming in Leoville and Efremovka because fluids could not penetrate the compacted rock. It is less clear whether the alkali-bearing phases can also be similarly attributed to parent body processes because minor secondary alkali-rich phases do occur in Efremovka and Leoville CAIs (e.g., E67-1; Fig. 3f). McGuire and Hashimoto (1989) presented independent arguments addressing why the alkali-bearing phases might be nebular rather than parent body in origin. The site where the alkali metasomatism took place, whether on a parent body or in the nebula, remains an open question.

Genetic Relationship to Type C CAIs

Figure 16 shows that the bulk compositions of spinel-rich, fine-grained CAIs largely overlap those of a relatively rare type of CAI known as type C, suggesting the possibility of a genetic relationship that we explore here. Type C CAIs are coarse-grained CAIs that are plagioclase-, pyroxene-, and

Table 5. Representative microprobe analyses of melilite in fine-grained CAIs from Efremovka and Leoville.

Ox\no	E101b-1		E103a		E67-1		E42		E49-a		E51	E14	L3536-1	
SiO_2	22.4	25.1	21.8	22.7	23.8	24.4	27.3	28.4	22.8	25.0	23.2	24.9	22.3	24.0
TiO_2	0.06	<0.05	0.14	<0.05	<0.05	<0.05	<0.05	<0.05	<0.05	<0.05	<0.05	0.03	<0.05	<0.05
Al_2O_3	35.6	31.9	35.8	34.5	34.1	32.7	27.3	25.8	35.6	32.0	34.7	31.6	34.8	33.2
Cr_2O_3	<0.07	<0.07	<0.07	0.00	<0.07	<0.07	<0.07	<0.07	<0.07	<0.07	<0.07	0.01	<0.07	<0.07
FeO	<0.08	0.09	0.18	0.34	0.26	<0.08	<0.08	<0.08	0.11	0.08	0.29	0.10	<0.08	0.11
MnO	<0.07	<0.07	<0.07	<0.07	<0.07	<0.07	<0.07	<0.07	<0.07	<0.07	<0.07	<0.07	<0.07	<0.07
MgO	0.83	2.2	0.41	0.93	1.3	1.7	3.9	4.6	0.71	2.0	1.1	2.2	0.42	3.0
CaO	40.5	40.6	40.4	40.6	40.5	41.2	40.1	40.5	41.1	40.3	40.5	41.8	40.5	39.1
Na_2O	<0.06	<0.06	<0.06	<0.06	<0.06	<0.06	0.07	<0.06	<0.06	<0.06	0.07	<0.06	<0.06	<0.06
Total	99.5	99.9	98.7	99.2	99.9	100.1	98.7	99.5	100.5	99.5	99.8	100.7	98.2	99.5
Structural formalue based on 7 O														
Si	1.028	1.145	1.008	1.049	1.086	1.114	1.259	1.300	1.037	1.142	1.062	1.134	1.040	1.098
Ti	0.002	–	0.005	–	–	–	–	–	–	–	–	0.001	–	–
Al	1.927	1.713	1.952	1.876	1.832	1.758	1.483	1.390	1.910	1.729	1.867	1.693	1.909	1.786
Cr	–	–	–	–	–	–	–	–	–	–	–	0.000	–	–
Fe	0.000	0.003	0.007	0.013	0.010	0.001	0.001	0.002	0.004	0.003	0.011	0.004	0.002	0.004
Mn	–	–	–	–	–	–	–	–	–	–	–	–	–	–
Mg	0.056	0.150	0.028	0.064	0.086	0.118	0.268	0.317	0.048	0.138	0.074	0.150	0.029	0.205
Ca	1.991	1.983	2.008	2.007	1.980	2.013	1.983	1.988	2.004	1.977	1.984	2.035	2.021	1.914
Na	–	–	–	–	–	–	0.007	0.005	–	–	0.006	0.000	–	–
Total	5.004	4.995	5.009	5.008	4.994	5.005	4.994	4.998	5.003	4.989	4.998	5.018	5.002	5.007
Ak	3.2	14.4	1.6	5.5	8.5	11.8	25.9	30.3	4.1	13.9	6.4	14.4	3.0	18.7

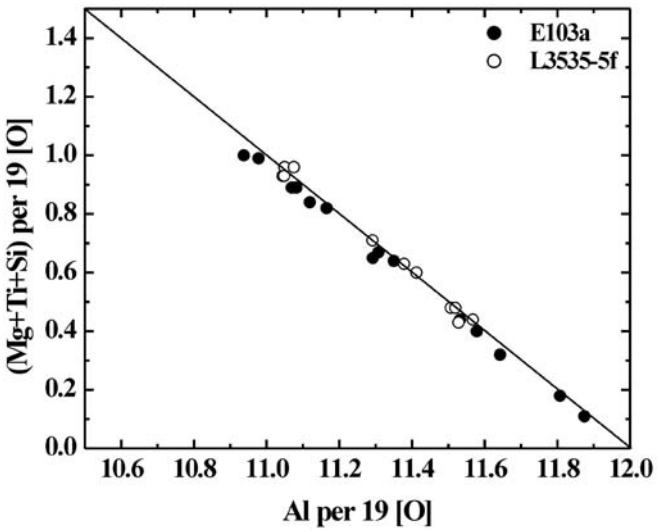

Fig. 11. Compositions of hibonite in the fine-grained, spinel-rich CAIs E103a and L3535-5f. Compositions are plotted as cations per 19 oxygens; see text for details.

Table 6. Representative microprobe analyses of forsterite in accretionary rims around fine-grained CAIs from Efremovka and Leoville.

Ox\CAI	E101b		L3536-1	L3535-5	
SiO_2	43.1	41.8	42.7	42.7	41.5
TiO_2	<0.05	<0.05	<0.05	<0.05	<0.05
Al_2O_3	<0.07	0.17	<0.07	<0.07	0.13
Cr_2O_3	0.11	0.08	0.08	<0.07	<0.07
FeO	0.75	3.8	0.98	0.27	3.7
MnO	<0.07	0.13	<0.07	<0.07	<0.07
MgO	57.4	54.9	56.1	56.9	54.1
CaO	0.13	0.08	0.30	0.32	0.15
Total	101.4	101.0	100.2	99.9	99.5
Structural formulae based on 4 O					
Si	0.998	0.987	1.003	1.000	0.993
Ti	–	–	–	–	–
Al	–	0.005	–	–	0.004
Cr	0.002	0.002	0.001	–	–
Fe	0.014	0.076	0.019	0.005	0.074
Mn	–	0.003	–	–	–
Mg	1.981	1.935	1.963	1.985	1.928
Ca	0.003	0.002	0.008	0.008	0.004
Total	3.001	3.010	2.996	3.000	3.005
Fa	0.7	3.8	1.0	0.3	3.7

spinel-rich but melilite- and olivine-poor (see Wark [1987] for a review). They typically have poikilitic or ophitic textures, indicating that the inclusions probably solidified from silicate melts. Type C CAIs have been described in several carbonaceous chondrite groups (Wark 1987).

Figure 16 also shows that the bulk compositions of type C CAIs, taken together with those of types A and B CAIs, define a combined trend that mimics but progressively deviates from the predicted trend for equilibrium solar nebula condensates. Type A CAIs plot on the predicted trend, but types B and C CAIs plot consistently above (to the corundum-rich, olivine-poor side) the condensation trend. Stolper (1982) discussed the significance of the predicted versus observed compositional trends in the context of type B CAIs, but in fact, the type C CAIs exhibit the greatest deviation from the predicted trend. Beckett and Grossman (1988) specifically considered the problem of type Cs and proposed a model in which the predicted equilibrium reactions (e.g., Grossman 1972) involving gehlenitic melilite + spinel to form åkermanitic melilite + pyroxene were kinetically inhibited relative to reactions in a silica-rich gas that produced pyroxene + anorthite instead.

Beckett and Grossman (1988) predicted that the precursors to type C CAIs were spinel-rich relative to types A or B CAIs and consisted of primary aluminous melilite (avg. $Åk_{17}$) + spinel (+ perovskite) solid condensates that had been altered to varying degrees to an assemblage of diopsidic pyroxene + anorthite. These are precisely the mineralogical attributes of fine-grained, spinel-rich inclusions from Efremovka and Leoville, as, in fact, Beckett and Grossman (1988) noted. Our bulk compositional data add further support to this connection between the two types of CAIs, as shown in Fig. 16. A similar conclusion has been reached by Lin and Kimura (1998) based on mineralogical and chemical studies of CAIs from Ninqiang. The link is even more direct for some type C inclusions that are known to possess group II trace element patterns (Wark 1987). Based on these observations and the lack of evidence for melting of fine-grained inclusions, we infer that the latter are probable precursors for type C CAIs.

Petrogenesis of Spinel-Rich, Fine-Grained Inclusions

General

All fine-grained, spinel-rich CAIs in Efremovka and Leoville, whether zoned or unzoned, have a basic internal structure in common, in which myriad small separate spinel nodules are rimmed by thin sequential layers of anorthite and pyroxene. Unlike the spinel grains, the pyroxene and anorthite layers commonly are continuous and enclose many spinels. The shapes of the spinel grains, and the nature of the spinel-anorthite and spinel-pyroxene contacts, indicate that the anorthite and pyroxene are replacing the spinel. The proportions of pyroxene to anorthite vary from inclusion to inclusion, but the structure is the same. This structure is present throughout the unzoned inclusions but is present primarily in the cores of the zoned, melilite-bearing inclusions. In the mantles of the zoned inclusions, melilite encloses the spinel and is itself rimmed and partially replaced by pyroxene and/or anorthite.

The critical point is that, in Efremovka and Leoville, the primary mineralogy and structures of the fine-grained, spinel-rich CAIs are not obscured by the morass of alkali- and iron-

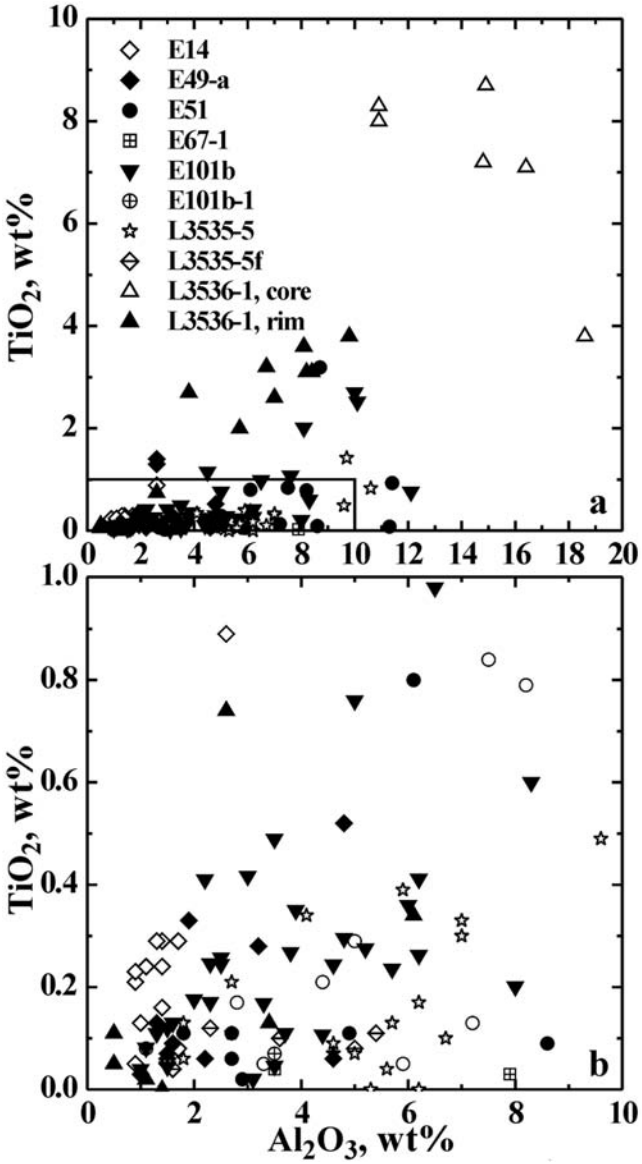

Fig. 12. Concentrations of TiO_2 versus Al_2O_3 (in wt%) in pyroxenes in fine-grained, spinel-rich CAIs from Efremovka and Leoville. The boxed area in the lower left of graph (a) is expanded in (b).

bearing alteration phases that is omnipresent in Allende. The pristine nature of the Leoville and Efremovka CAIs permits insights about their origin that cannot be gleaned from the heavily altered Allende inclusions. For example, Kornacki and Wood (1985) used the almost complete lack of melilite from the Allende spinel-rich inclusions that they studied to argue against a condensation origin. However, the primary internal structures are revealed in the Leoville and Efremovka CAIs to consist of sequences of monomineralic layers that cannot be the products of melt solidification, refuting previous interpretations to the contrary (e.g., Kornacki and Wood 1985). These layered microstructures have the attributes of reaction zones, and the group II trace element signatures of the bulk inclusions and their constituent phases (Huss et al. 2002) imply that the reactions were between solids and the nebular gas. The enrichment of fine-grained CAIs in the light isotopes of magnesium (Brigham et al. 1985, 1986) implies that the nature of these gas-solid reactions was condensation not evaporation. These inclusions, therefore, can be viewed as case studies of real nebular condensation processes "caught in the act." By comparing the inferred reactions with those predicted by equilibrium thermodynamics, it is clear that the real process differed significantly from equilibrium condensation. The observed textures clearly show that reactions did not go to completion; thus, the condensation was fractional rather than equilibrium. Moreover, this stage of condensation apparently proceeded by heterogeneous nucleation and surface-reaction on early-formed grains; thus, the reactions were limited by diffusion as reaction rims protected the underlying grains from further reaction (e.g., Petaev and Wood 1998a). Finally, many of the observed reactions and mineral sequences in these inclusions are not predicted by either equilibrium or fractional condensation.

In the following section, we examine the properties of the inclusions in light of the predictions of equilibrium condensation calculations, inferring both the genesis of the inclusions and the details of the evolving condensation process. The origin of the macro-scale zonation of many of the CAIs is considered separately, in the subsequent section, because evidence detailed therein suggests that the melilite-rich mantles post-date the fine-grained reaction textures recorded in the inclusion interiors.

The Record of Condensation in Fine-Grained, Spinel-Rich Inclusions: Observation Versus Theory

The texturally inferred crystallization sequence (order of appearance) of minerals within the fine-grained, spinel-rich CAIs we studied is: perovskite → hibonite → spinel → melilite → Al-diopside → anorthite → forsterite, although not all phases occur in all inclusions. This sequence is based mostly on stratigraphic position, with the exception of anorthite and pyroxene only. Where those two layers occur together, the anorthite layer underlies (stratigraphically precedes) the pyroxene layer. However, anorthite is absent from some inclusions (Fig. 1) or their individual layers (Fig. 2f) and replaces melilite in others (Figs. 2e and 2f), suggesting that the anorthite actually postdates formation of Al-diopside. In any event, the overall crystallization sequence is inconsistent with the predicted equilibrium condensation sequence from either a canonical solar gas or a dust-enriched system (considering here only those phases of relevance to spinel-rich inclusions): hibonite → perovskite → melilite → spinel → Al-diopside → forsterite → anorthite (Grossman 1972; Yoneda and Grossman [1995] Wood and Hashimoto 1993; Petaev and Wood 1998a; Ebel and Grossman 2000; Petaev et al. 2003). At a total pressure of 10^{-4} atm (using the calculations of Yoneda and

Table 7. Bulk compositions of fine-grained CAIs in Efremovka and Leoville normalized to 100%.

CAI	Location	Vol. fr.[a]	No. an.	SiO_2	TiO_2	Al_2O_3	Cr_2O_3	FeO	MnO	MgO	CaO	Na_2O	K_2O
E101b-1	Bulk	1	74	25.5	0.42	35.5	0.12	0.84	<0.08	14.9	22.5	0.16	n.a.[b]
E46-a	Bulk	1	39	24.4	2.1	36.7	0.15	3.5	<0.08	16.7	16.3	0.11	<0.04
L3535-5f	Bulk	1	56	23.7	0.76	43.6	<0.07	3.1	<0.08	13.6	15.1	<0.08	n.a.
E103a	Core	0.41	136	26.9	0.60	42.5	0.13	0.76	<0.08	15.7	13.3	<0.08	n.a.
	Mantle	0.59	160	19.9	0.70	43.1	0.08	1.5	<0.08	11.2	23.4	0.14	n.a.
	Bulk	1	–	22.8	0.66	42.9	0.10	1.2	<0.08	13.1	19.3	<0.08	n.a.
E67-1	Core	0.21	190	37.3	0.69	37.5	<0.07	0.53	<0.08	5.5	18.0	0.35	n.a.
	Mantle	0.79	148	36.0	0.57	30.8	<0.07	0.68	<0.08	6.3	25.4	0.11	n.a.
	Bulk	1	–	36.3	0.60	32.2	<0.07	0.65	<0.08	6.1	23.9	0.16	n.a.
E42	Core	0.05	182	30.4	2.1	38.5	0.38	0.48	<0.08	12.4	15.6	<0.08	<0.04
	Mantle	0.95	106	37.0	0.69	22.8	0.13	0.30	<0.08	10.9	28.1	0.09	<0.04
	Bulk	1	–	35.2	1.1	27.1	0.20	0.35	<0.08	11.3	24.7	0.08	<0.04
E49-a[c]	Core	0.22	69	32.4	1.5	35.4	0.48	0.79	<0.08	14.9	14.4	<0.08	n.a.
	Mantle	0.78	87	32.8	1.0	25.7	0.10	1.1	<0.08	9.6	29.7	<0.08	n.a.
	Bulk	1	–	32.7	1.1	27.9	0.18	1.0	<0.08	10.7	26.3	<0.08	n.a.
E51	Core inner	0.046	103	26.8	1.0	39.6	0.26	0.59	<0.08	19.2	12.5	<0.08	<0.04
	Core, outer	0.31	97	30.7	1.0	42.4	0.24	0.65	<0.08	11.0	13.9	0.10	<0.04
	Mantle	0.639	53	37.1	0.92	28.5	0.15	1.2	<0.08	14.8	17.2	0.10	<0.04
	Bulk	1	–	34.6	0.96	33.4	0.18	1.0	<0.08	13.8	15.9	0.10	<0.04
E14	Core	0.048	138	30.4	0.26	35.6	0.62	0.95	<0.08	19.7	12.4	<0.08	<0.04
	Mantle	0.95	135	41.0	0.34	23.0	0.33	0.80	<0.08	16.3	18.1	<0.08	<0.04
	Bulk	1	–	40.5	0.34	23.6	0.35	0.81	<0.08	16.4	17.9	<0.08	<0.04
E101b	Core	0.229	168	30.7	0.41	37.9	0.37	0.87	<0.08	15.8	13.8	0.17	<0.04
	Mantle	0.771	140	38.2	0.60	25.4	0.22	1.8	<0.08	17.1	16.5	0.20	<0.04
	Bulk	1	–	36.5	0.56	28.3	0.25	1.6	<0.08	16.8	15.9	0.19	<0.04
E71	Bulk	1	203	33.2	0.56	35.5	0.17	1.1	<0.08	14.3	15.1	<0.08	<0.04
L3536-1	Core	0.17	–	30.3	1.2	34.8	n.a.	0.53	<0.08	14.2	17.0	0.19	n.a.
	Mantle	0.83	–	31.1	0.45	30.0	n.a.	0.91	<0.08	13.0	23.2	0.17	n.a.
	Bulk	1	–	31.0	0.57	30.8	n.a.	0.84	<0.08	13.1	22.5	0.18	n.a.

[a]Vol. fr. = volume fraction.
[b]n.a. = not analyzed.
[c]Compound inclusion; only the bulk compositions of the fine-grained inclusion are listed.

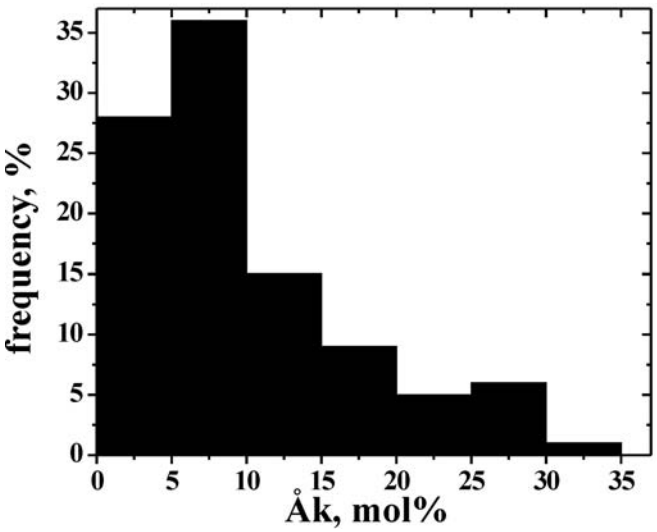

Fig. 13. Histogram showing the åkermanite (Åk) contents (mol% $Ca_2MgSi_2O_7$) of melilite in fine-grained, spinel-rich CAIs from Efremovka and Leoville.

Grossman [1995] as an example), hibonite is predicted to begin condensing at 1647 K at the expense of earlier-formed corundum. Perovskite condenses at 1609 K. Melilite begins condensing at 1546 K through a reaction between hibonite and the nebular gas. Spinel begins forming at 1421 K, more than 100 K lower than the first appearance of melilite, at the expense of hibonite that has not completely reacted to form melilite. Spinel continues forming at a still-lower temperature through a second reaction between melilite and gaseous Mg. Diopside forms 40–50 K below the first appearance of spinel, owing to a reaction between melilite and spinel. Forsterite first appears just below the temperature at which diopside first appears. Anorthite forms through a reaction of spinel with diopside at a temperature approximately 30 K lower than the first appearance of forsterite.

The major inconsistencies between the above predictions of equilibrium thermodynamics and the observations in the fine-grained, spinel-rich inclusions are: 1) the relative sequence of perovskite with respect to hibonite; 2) the relative sequence of spinel with respect to melilite and hibonite; and 3) the relative sequence of anorthite with respect to forsterite.

In the following paragraphs, we discuss, in the order noted at the beginning of this section, the crystallization sequence and reactions recorded in the fine-grained CAIs in the context of the condensation predictions. One of the most important conclusions we reach is that, although the second of the inconsistencies noted above has received the most attention in the literature, it is the third discrepancy (anorthite condensation relative to that of forsterite) that may be the

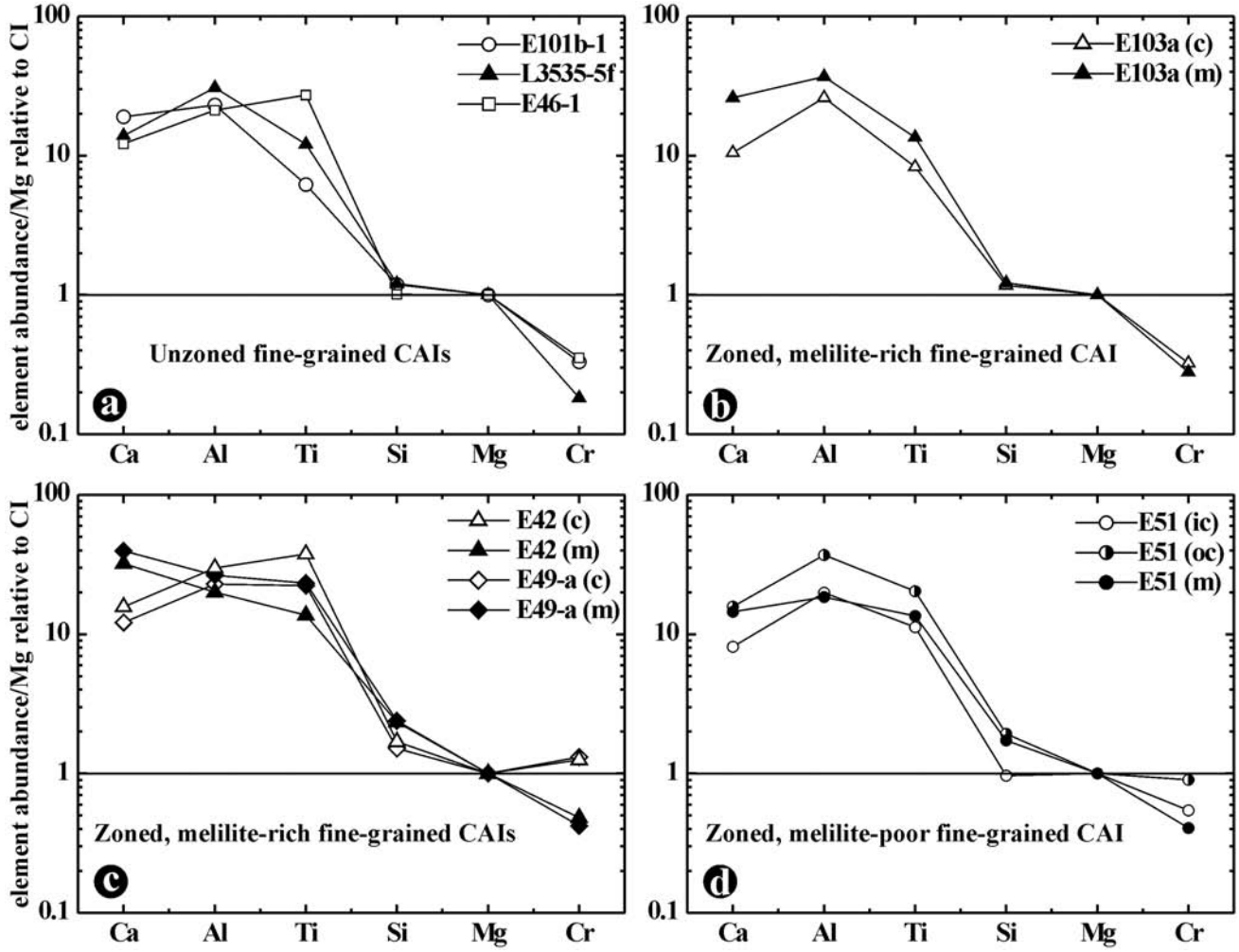

Fig. 14. Bulk compositions of (a) unzoned, (b and c) zoned, melilite-rich, and (d) zoned, melilite-poor fine-grained, spinel-rich CAIs from Efremovka and Leoville. The compositions are normalized to Mg and CI chondrite abundances. For clarity, only a representative sampling of the studied CAIs is plotted.

most important in understanding the bulk chemistry not only of these but also many other CAI varieties.

The enclosing of perovskite within hibonite has been cited as one argument against a nebular condensation origin for fine-grained, spinel-rich inclusions (Kornacki and Fegley 1984; Kornacki and Wood 1985). However, recent trace element studies (Huss et al. 2002) on some of the CAIs described in this work, using an ion microprobe, show that individual perovskite grains in the inclusion interiors possess group II trace element patterns that fingerprint the condensation process (Boynton 1975; Davis and Grossman 1979). If the perovskite and its enclosing hibonite are not actual nebular condensates, then they must have recrystallized isochemically from material that was a condensate. Nevertheless, no plausible mechanism has yet been proposed for how perovskite might condense at a higher temperature than hibonite. Fractional condensation is an unlikely explanation because it has very little effect on the temperature of the first appearance of a phase and raises rather than lowers the temperature of the disappearance of a phase (Petaev and Wood 1998a). There is no obvious reason for why hibonite nucleation would be kinetically suppressed relative to that of perovskite. This discrepancy between theory and observation remains unexplained.

The inconsistency between the observed versus predicted crystallization sequence of spinel and melilite has been widely discussed in the CAI literature and has been cited as evidence that fine-grained, spinel-rich inclusions, in particular, cannot be aggregates of nebular condensates (Kornacki and Fegley 1984). These authors proposed, for example, that fine-grained, spinel-rich inclusions must, instead, have formed from spinel-rich partial melts in which a spinel-rich solid residue was left behind following the loss of residual liquid by a combination of collision-induced filter-pressing and melt evaporation. This hypothesis appears to be inconsistent with mass-dependent isotope fractionation of Mg favoring light rather than heavy isotopes (Δ^{25}Mg, ranges from 2‰ down to −26‰ per amu) in Allende fine-grained, spinel-

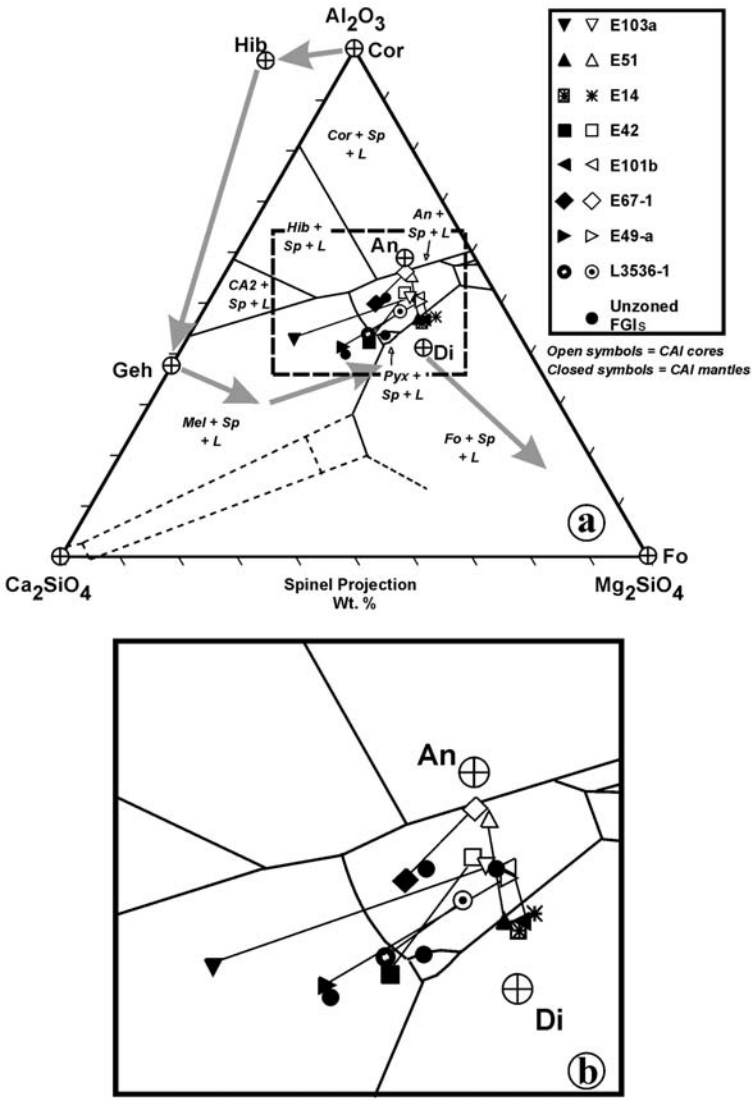

Fig. 15. a) Compositions of the cores and mantles of fine-grained, spinel-rich CAIs from Efremovka and Leoville, projected from spinel onto the plane Ca_2SiO_4-Mg_2SiO_4 (forsterite; Fo) -Al_2O_3 (corundum; Cor), together with the spinel-saturated liquidus relationships in this system (see MacPherson and Huss [2000] for an explanation of this diagram and calculation of the plotting coordinates); grey vectors show the calculated trajectory for bulk solids during high temperature equilibrium condensation of a solar composition gas (Yoneda and Grossman 1995). The core and mantle compositions of each inclusion are joined by solid lines; b) an enlargement of the central portion of (a).

rich inclusions, suggesting that they (or their immediate precursors) are either early condensates or re-condensates from distillation of coarse-grained CAIs (Brigham et al. 1985, 1986). Magnesium isotope compositions of fine-grained, spinel-rich inclusions from Efremovka and Leoville have yet to be measured. In addition, the group II REE patterns reported for Allende (Brigham et al. 1985, 1986) and Efremovka and Leoville (Mao et al. 1990; Huss et al. 2002) fine-grained inclusions appear to mandate a condensation origin. If they are condensates, then how can the observations be reconciled with theory? Beckett and Stolper (1994) showed independent evidence that melilite condensation might have been depressed to lower temperatures: some hibonite- and corundum-bearing but melilite-free assemblages have equilibration temperatures below the equilibrium condensation temperature of melilite. Those authors suggested two mechanisms that might have caused this suppression of melilite condensation to a temperature below that of spinel condensation. One is that heterogeneous nucleation of spinel was favored on some structurally compatible surfaces of hibonite crystals, while that of melilite was not. The result was that melilite substantially overshot its condensation temperature, while spinel did not. The one difficulty is that the required undercooling for melilite condensation, ~100 K, may be unreasonably large. Another problem with this hypothesis is that the condensation of melilite by the reaction of hibonite with gaseous SiO does not require Ca evaporation, but that of spinel does. Beckett and

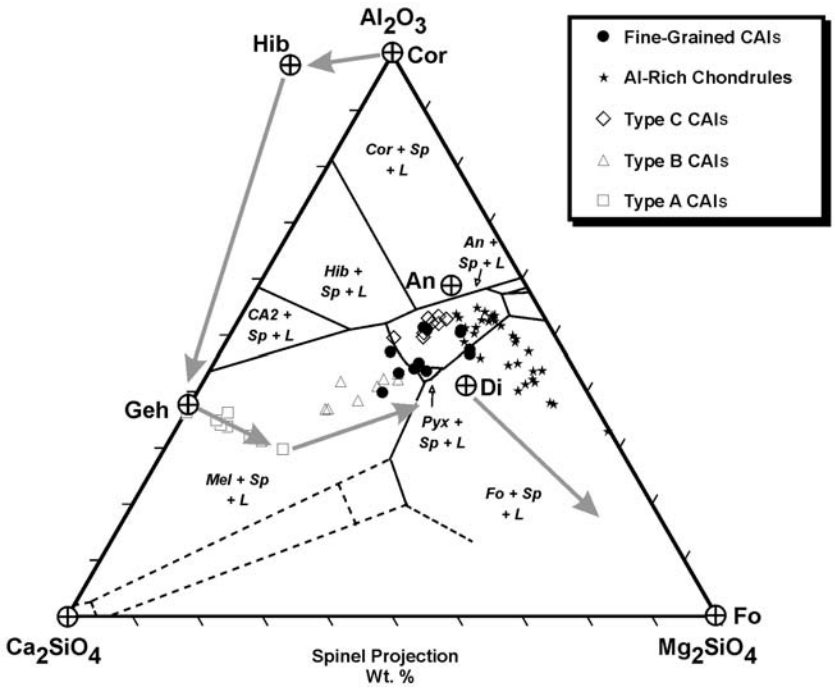

Fig. 16. Bulk compositions of fine-grained, spinel-rich CAIs from Efremovka and Leoville plotted as in Fig. 15; also shown are the compositions of Al-rich chondrules (data from Bischoff and Keil 1984; Sheng et al. 1991) and types A, B, and C CAIs (data from Beckett 1986; Wark 1987) and the calculated trajectory for bulk condensed solids during equilibrium condensation (Yoneda and Grossman 1995).

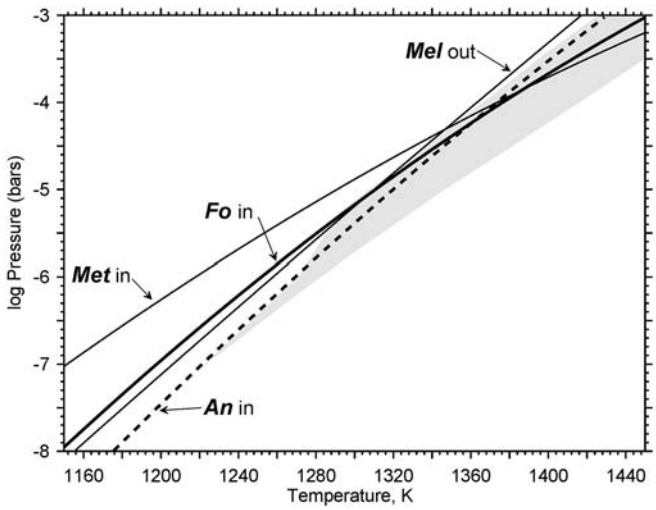

Fig. 17. Equilibrium condensation curves of some minerals in a system of solar composition. The labels on the curves correspond to the appearance of forsterite (Fo in), anorthite (An in), and Fe-Ni metal (Met in) and the disappearance of melilite (Mel out). The stability field of spinel is shaded. The forsterite-metal and anorthite-forsterite reversals occur at ~7×10^{-5} bar and 5×10^{-5} bar, respectively.

Stolper (1994) suggested an alternative possibility, in which extreme fractional condensation of a highly aluminous phase (corundum or hibonite) resulted in a nebular gas that was anomalously depleted in aluminum, thus suppressing the equilibrium condensation of melilite until after spinel had appeared. However, this second model appears unlikely because the results of Petaev and Wood (1998a) suggest that even large degrees of fractional condensation have little effect on the condensation temperature of melilite, while spinel entirely disappears from the condensation sequence. There is also the problem that most fine-grained, spinel-rich inclusions show significant depletion in Ca relative to Al (Fig. 14), which is difficult to reconcile with both condensation from a gas of solar composition and condensation from an aluminum-depleted gas.

The presence of an aluminous diopside layer in direct contact with melilite, and the apparent inverse correlation between the thicknesses of these two layers (Fig. 1), is broadly consistent with the predicted reaction between melilite and gaseous Mg and SiO to form pyroxene, except for the absence (in the mantles of zoned inclusions) of spinel as a participant. (see also Lin and Kimura 1998, 2003). The observed reactions can be written as:

$$\text{(Mantle) } Ca_2Al_2SiO_7 + Mg(g) + 2SiO(g) + 3H_2Og = (CaAl_2SiO_6 + CaMgSi_2O_6) \text{ (pyroxene solid solution)} + 3H_2(g) \quad (1)$$

$$\text{(Core) } 3Ca_2Al_2SiO_7 + MgAl_2O_4 + Mg(g) + 5SiO(g) + 6H_2O(g) = (4CaAl_2SiO_6 + 2CaMgSi_2O_6) \text{ (pyroxene solid solution)} + 6H_2(g) \quad (2)$$

Reaction 2 is consistent with the observation that pyroxene in the cores of the zoned CAIs is enriched in Al (and Ti) relative to pyroxene in the mantle, reflecting the participation of spinel (which is more abundant in the CAI cores) and some perovskite in the reaction. If rewritten to include perovskite,

Reaction 2 is the pyroxene-forming reaction predicted by Yoneda and Grossman (1995).

Forsterite is mostly lacking in the interiors of spinel-rich, fine-grained inclusions, yet equilibrium condensation calculations generally predict that forsterite should condense at a higher temperature than the ubiquitous anorthite. Why is forsterite missing from the interiors of these condensate inclusions? This particular disconnect between equilibrium condensation calculations and observations of natural CAIs is a problem that has not been fully appreciated, yet it may be an important factor in understanding the bulk compositions of types B and C CAIs relative to the predictions of equilibrium condensation. In essence, many CAIs are more anorthite-normative and forsterite-deficient than expected. Beckett and Grossman (1988) explicitly addressed the issue in trying to explain the bulk compositions of type C inclusions; MacPherson and Huss (2000) extended the argument to type B CAIs as well. Beckett and Grossman (1988) proposed that the condensate precursors to type C CAIs experienced a reaction between melilite, spinel, and silica-rich gas to form anorthite + pyroxene. This reaction must occur at a higher temperature than the predicted equilibrium condensation of forsterite. The assemblages in fine-grained, spinel-rich CAIs are broadly consistent with the model of Beckett and Grossman (1988), although, in the mantles of the zoned inclusions, the reaction apparently was melilite alone reacting with a silica-rich gas to form anorthite + pyroxene:

$$Ca_2Al_2SiO_7 + 3SiO(g) + Mg(g) + 4H_2O(g) = CaAl_2Si_2O_8 + CaMgSi_2O_6 + 4H_2(g) \quad (3)$$

An interesting new alternative explanation for the lack of forsterite in fine-grained CAIs involves their condensation at low nebular pressures. Petaev and Wood (1998b) first showed that the condensation sequence of forsterite and anorthite is pressure-dependent; i.e., anorthite condenses before forsterite at nebular pressures below ~2.5×10^{-8} bar. But, they concluded that such a low pressure of the anorthite-forsterite reversal may be unrealistic for the early solar nebula. Our newer calculations, using a revised version of the condensation with partial isolation (CWPI) code (Petaev et al. 2003), and based on a self-consistent thermodynamic database, indicate that the forsterite-anorthite reversal occurs at much higher nebular pressures than suggested by Petaev and Wood (1998b), ~5×10^{-5} bar (Fig. 17); the temperature gap between anorthite and forsterite increases with falling nebular pressure. MacPherson et al. (2004) showed that, if condensation did take place at nebular pressures under which anorthite condensation precedes that of forsterite, the bulk composition trajectory predicted by such condensation much more closely overlaps the trajectory defined by the bulk compositions of types A, B, and C CAIs than that of earlier condensation calculations (e.g., Yoneda and Grossman 1995). Thus, this model may explain not only the fine-grained, spinel-rich inclusion properties but also resolve a long-standing puzzle regarding many other CAI varieties.

In summary, the sequence of condensation and reactions that is recorded by the sequential micro-layering in the interiors of fine-grained, spinel-rich inclusions is:

1. Condensation of perovskite;
2. Condensation of hibonite;
3. Condensation of spinel;
4. Formation of melilite through a reaction between spinel and gas;
5. Formation of pyroxene through a reaction between melilite (and spinel) with a silica- and magnesium-rich gas;
6. Formation of anorthite and additional pyroxene through a reaction of melilite and spinel with a silica- and magnesium-rich gas.

Origin of Macro-Scale Zonation

The large-scale melilite-rich mantles of the structurally zoned inclusions cannot easily be reconciled with the single sequence of condensation and reaction events as outlined above. The commonly multiple concentric zones (e.g., Leoville 3536-1; see Fig. 4d), the diffuse nature of the boundaries between the zones, and the fact that the layering parallels the shapes of even very irregular inclusions all suggest that the macro-scale structural zoning post-dates the assembly of the inclusions and the formation of the tiny multi-rimmed, spinel-rich nodules.

There is one conceivable way in which these mantles could have formed contemporaneously with the process outlined above. Before the onset of any melilite formation, the inclusions were simple porous aggregates of spinel, perovskite, and, in some cases, hibonite. If, as the cooling nebular gas permeated the inclusions, condensation of melilite occurred first at the CAI margin through heterogeneous nucleation onto spinel surfaces, then continued melilite condensation preferentially on the CAI exteriors could have sealed off the CAI interiors from further reaction. Subsequent condensation of melilite on the CAI outer surface would then lead to a thick melilite mantle outside of a relatively melilite-deficient interior. This model has two serious problems, however. First, the existence of anorthite and pyroxene in the interiors of the CAIs, formed during a subsequent stage of inclusion evolution, means that the gas did, in fact, have access to the CAI interiors—they were not completely sealed. Second, such a model does not, by itself, explain how the unzoned, fine-grained inclusions escaped the formation of melilite.

Three other models can be considered for the origin of the melilite-rich outer mantles, all of which involve those mantles forming later by a separate process: 1) late accretion or condensation of melilite-rich materials onto the melilite-poor cores; 2) partial melting of the inclusion exteriors accompanied by melt evaporation and recrystallization; or 3)

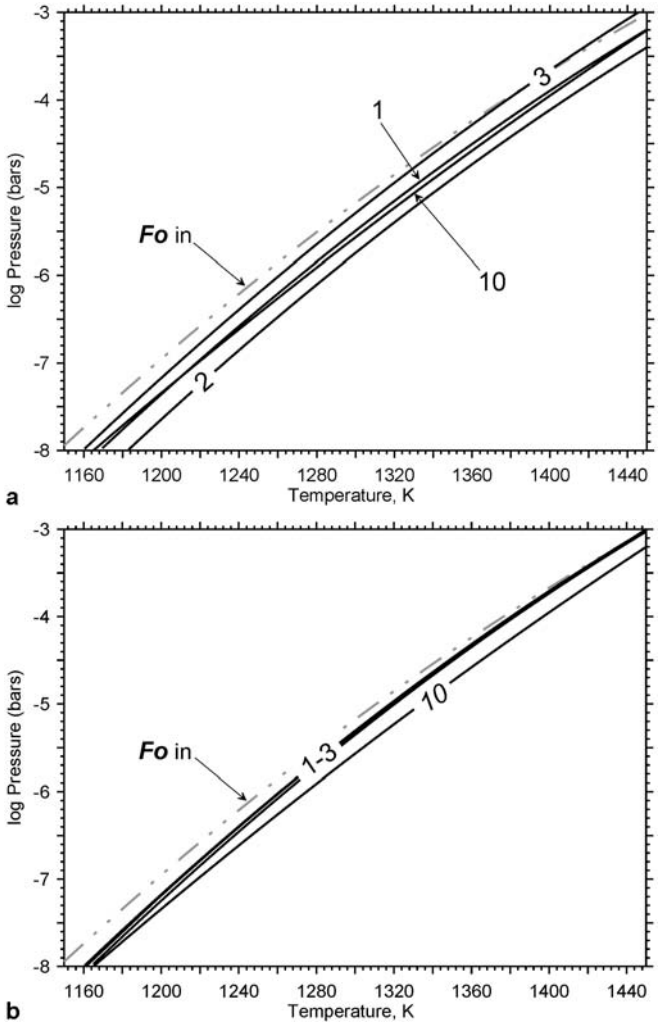

Fig. 18. Phase boundaries of Reactions 1–3 and 10 in equilibrium with the residual nebular gas in a system of the solar composition. The labels on the curves are the reaction numbers. The stability fields of melilite are on the right-hand sides of the curves. The dashed-dotted gray line shows the first appearance of forsterite (Fo in): a) the compositions of coexisting melilite and clinopyroxene are ($Ge_{95}Åk_5$) and ($Di_{95}CATS_5$), respectively; b) the compositions of coexisting melilite and clinopyroxene are ($Ge_{95}Åk_5$) and ($Di_{80}CATS_{20}$), respectively. See discussion in the text.

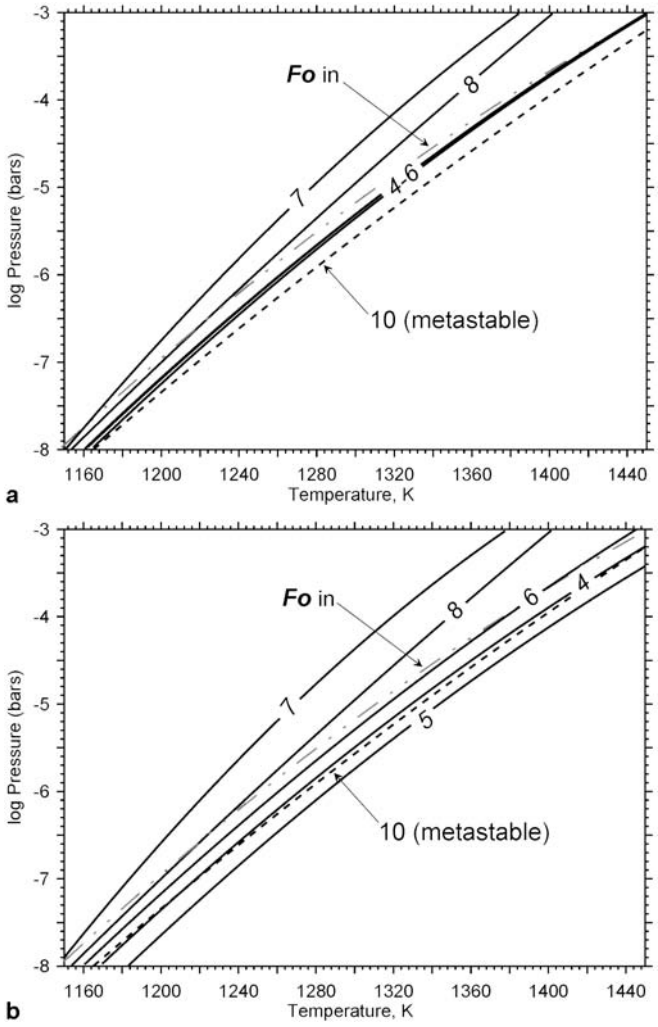

Fig. 19. Phase boundaries of Reactions 4–8 and 10 in equilibrium with the residual nebular gas in a system of the solar composition. The labels on the curves are the reaction numbers. The stability fields of melilite are on the right-hand sides of the curves. The dashed-dotted gray line shows the first appearance of forsterite (Fo in): a) the compositions of coexisting melilite and clinopyroxene are ($Ge_{95}Åk_5$) and ($Di_{80}CATS_{20}$), respectively; b) the compositions of coexisting melilite and clinopyroxene are ($Ge_{95}Åk_5$) and ($Di_{95}CATS_5$), respectively. See discussion in the text.

solid-to-gas evaporation and recrystallization. As in the model already described, none of these three is without problems.

The diffuse contact between the mantle and core in the structurally zoned inclusions argues against the mantle being added later by simple physical accretion of melilite-rich material. If this material was added later, it must have been by condensation/reaction. However, there are three arguments against condensation of melilite-rich material subsequent to the formation of the spinel-rich inclusion cores: 1) as with the first model noted above, this one cannot, by itself, explain the existence of melilite-poor and mineralogically unzoned, fine-grained inclusions in CVs (e.g., Fig. 1) and other chondrites groups (Holmberg and Hashimoto 1992; MacPherson and Davis 1994; Hashimoto et al. 2001; Krot et al. 2001; Alèon et al. 2002; Fagan et al. 2000); 2) such a second stage of melilite condensation requires the wholesale transport of the inclusions to a higher temperature region of the nebula than that in which the earlier-formed anorthite and pyroxene in the CAI core were formed; and 3) the observation (Huss et al. 2002) that the mantle melilite possesses a group II trace element signature requires that the putative second stage of condensation also occurred in a nebular region that had already experienced a prior condensation episode in which the most refractory lithophile elements were removed. We infer that the decrease in volatility and increase in grain size toward the CAI peripheries likely reflects thermal processing (re-heating) and surficial

volatilization of fine-grained inclusions after their initial formation as uniform aggregates of spinel-cored nodules.

Such volatilization might have occurred from a melt. However, there is no support for the idea that fine-grained, spinel-rich inclusions were melted at all, much less melted and evaporated. As shown earlier in Fig. 16, the bulk compositions of spinel-rich, fine-grained CAIs plot in the anorthite + spinel primary phase volume for melt-solid phase equilibria. Melts of such bulk compositions will crystallize spinel or anorthite first, generally followed by pyroxene. The resulting solids are expected to have poikilitic or ophitic textures, such as those in type C CAIs. Fine-grained, spinel-rich inclusions have neither the expected textures nor the correct crystallization sequence, indicating that these inclusions were not extensively (if at all) melted. Moreover, if formation of the CAI macro-zoning was due to partial melting and evaporation through a Rayleigh-like process, mass-dependent isotopic fractionation of Mg, O, and Si isotopes should be observed: the melilite-rich mantle of an inclusion is expected to be enriched in heavy isotopes relative to a spinel-rich core. Although no Mg isotope measurements of zoned, fine-grained inclusions from Efremovka and Leoville have been done yet, it was found that bulk fine-grained inclusions in Allende are enriched in light Mg isotopes instead (Brigham et al. 1985, 1986). Finally, the REE patterns of coexisting minerals in the core and mantle of two zoned, fine-grained inclusions in Efremovka are inconsistent with igneous partitioning (Huss et al. 2002).

Finally, we consider the possibility that surficial volatilization of the zoned CAIs occurred by sublimation. Assuming that the precursor objects had exactly the mineralogy and textures of the CAI cores—tiny spinel-cored nodules surrounded by layers of anorthite and pyroxene—the melilite could have formed in any of three ways: 1) by reactions opposite to Reactions 1–3:

$$(CaAl_2SiO_6 + CaMgSi_2O_6)\ (pyx\ ss) + 3H_2(g) = Ca_2Al_2SiO_7 + Mg(g) + 2SiO(g) + 3H_2O(g) \quad (4)$$

$$(4CaAl_2SiO_6 + 2CaMgSi_2O_6)\ (pyx\ ss) + 6H_2(g) = 3Ca_2Al_2SiO_7 + MgAl_2O_4 + Mg(g) + 5SiOg + 6H_2O(g) \quad (5)$$

$$CaAl_2Si_2O_8 + CaMg_2Si_2O_6 + 4H_2(g) = Ca_2Al_2SiO_7 + 3SiO(g) + Mg(g) + 4H_2O(g) \quad (6)$$

2) by reaction between diopside and spinel:

$$4CaMgSi_2O_6 + MgAl_2O_4 + 9H_2(g) = Ca_2Al_2SiO_7 + Ca_2MgSi_2O_7 + 4Mg(g) + 5SiO(g) + 9H_2O(g) \quad (7)$$

3) or by reactions between spinel and anorthite:

$$CaAl_2Si_2O_8 + MgAl_2O_4 + 5Ca(g) + 2SiO(g) + 7H_2O(g) = 2Ca_2Al_2SiO_7 + Ca_2MgSi_2O_7 + 7H_2(g) \quad (8)$$

$$CaAl_2Si_2O_8 + MgAl_2O_4 + 4Ca(g) + 2SiO(g) + 6H_2O(g) = 2Ca_2Al_2SiO_7 + CaMgSi_2O_6 + 6H_2(g) \quad (9)$$

$$CaAl_2Si_2O_8 + MgAl_2O_4 + 3Ca(g) + 2H_2O(g) = 2Ca_2Al_2SiO_7 + Mg(g) + 2H_2(g) \quad (10)$$

There is no clear textural basis for preferring one or more of these reactions over any of the others. Accordingly, we used thermodynamic calculations to evaluate the relative stabilities of each of these reactions. In addition, we also explored the physicochemical conditions that would enable Reactions 1–3 to proceed.

Our thermodynamic calculations, discussed in detail in the Appendix, indicate that replacement of melilite by anorthite, spinel, and pyroxene solid solution (Reactions 1–3 and 10; Fig. 18) occurs during continuous cooling, before condensation of forsterite, and continues until melilite disappears completely. The formation of melilite-rich mantles of the zoned inclusions by the evaporative loss of Mg and Si (Reactions 4–8; Fig. 19) is essentially reciprocal to the sequence of alteration reactions of melilite under continuous cooling.

CONCLUSIONS

1. Fine-grained, spinel-rich inclusions in the reduced CV chondrites Efremovka and Leoville consist of spinel, melilite, anorthite, Al-diopside, and minor hibonite and perovskite; forsterite is very rare. Several inclusions are surrounded by forsterite-rich accretionary rims. In contrast to heavily altered and highly porous fine-grained, spinel-rich inclusions in the oxidized CV chondrite Allende, those in Efremovka and Leoville experienced very little alteration and are relatively compact. They lack hedenbergite, andradite, grossular, wollastonite, and ferrous olivine; secondary nepheline and sodalite are rare.
2. Three out of the 13 fine-grained inclusions studied are mineralogically uniform and consist of the concentrically zoned nodules having a spinel ± hibonite ± perovskite core surrounded by the layers of melilite and Al-diopside. Most inclusions, however, show an overall mineralogical zoning with a distinct core-mantle structure. The core is melilite-free and consists of the concentrically zoned objects having a spinel ± hibonite ± perovskite core surrounded by the layers of anorthite and Al-diopside. The mantle is Ca-enriched, Mg-depleted, and coarser-grained relative to the core; it is melilite-rich and contains less spinel and anorthite than the core. The bulk compositions of fine-grained inclusions are similar to those of coarse-grained igneous, type C CAIs and show significant fractionation of Al from Ca and Ti, with Ca and Ti being depleted relative to Al; a degree of depletion decreases toward the CAI periphery. The Efremovka CAI E49-a is a compound object with an inner portion composed of a zoned, fine-grained, spinel-rich inclusion and an outer portion composed of a

melilite-rich (type A) CAI. Fine-grained, spinel-rich inclusions are characterized by ^{16}O-rich isotopic compositions of primary minerals (Aléon et al. 2002), are enriched in light Mg isotopes (Brigham et al. 1985), and have group II REE patterns (Huss et al. 2002).

3. We conclude that fine-grained, spinel-rich inclusions originally formed as aggregates of spinel-perovskite-melilite ± hibonite gas-solid condensates from an ^{16}O-enriched gaseous reservoir depleted in refractory REEs. These aggregates later experienced low temperature gas-solid nebular reactions with gaseous SiO and Mg to form Al-diopside and ±anorthite. The zoned, fine-grained inclusions subsequently experienced re-heating that resulted in the loss of SiO and Mg and the formation of melilite. Melting of some of the fine-grained, spinel-rich inclusions can explain the existence of coarse-grained type C CAIs that have group II trace element signatures. The inferred multi-stage formation history of fine-grained, spinel-rich inclusions in Efremovka and Leoville is consistent with a complex formation history of coarse-grained CAIs in CV chondrites.

Acknowledgments–This work was supported by NASA grants NAG5–10610 (A. N. Krot, P. I.), NAG5–10468 (G. J. MacPherson, P. I.), and NAG5–11591 (K. Keil, P. I.). We thank Drs. A. El Goresy, J. Paque, and E. K. Zinner for constructive reviews that significantly improved the manuscript. This is Hawai'i Institute of Geophysics and Planetology publication No. 1345 and School of Ocean and Earth Science and Technology publication No. 6468.

Editorial Handling—Dr. Ernst Zinner

REFERENCES

Aléon J., Krot A. N., and McKeegan K. D. 2002. Ca-Al-rich inclusions and amoeboid olivine aggregates from the CR carbonaceous chondrites. *Meteoritics & Planetary Science* 37: 1729–1755.

Beckett J. R. and Grossman L. 1988. The origin of type C inclusions from carbonaceous chondrites. *Earth and Planetary Science Letters* 89:1–14.

Beckett J. R. and Stolper E. 1994. The stability of hibonite, melilite, and other aluminous phases in silicate melts: Implications for the origin of hibonite-bearing inclusions from carbonaceous chondrites. *Meteoritics* 29:41–65.

Berman R. G. 1988. Internally consistent thermodynamic data for minerals in the system Na_2O-K_2O-CaO-MgO-FeO-Fe_2O_3-Al_2O_3-SiO_2-TiO_2-H_2O-CO_2. *Journal of Petrology* 29:445–522.

Boynton W. V. 1975. Fractionation in the solar nebula: Condensation of yttrium and the rare earth elements. *Geochimica et Cosmochimica Acta* 39:569–584.

Boynton W. V., Wark D. A., and Ulyanov A. A. 1986. Trace elements in Efremovka fine-grained inclusion E14: Evidence for high temperature, oxidizing fractionations in the solar nebula (abstract). 17th Lunar and Planetary Science Conference. pp. 78–79.

Brigham C. A., Papanastassiou D. A., and Wasserburg G. J. 1985. Mg isotopic heterogeneities in fine-grained, Ca-Al-rich inclusions (abstract). 16th Lunar and Planetary Science Conference. pp. 93–94.

Brigham C. A., Hutcheon I. D., Papanastassiou D. A., and Wasserburg G. J. 1986. Evidence for ^{26}Al and Mg isotopic heterogeneity in a fine-grained CAI (abstract). 17th Lunar and Planetary Science Conference. pp. 85–86.

Charlu T. V., Newton R. C., and Kleppa O. J. 1981. Thermochemistry of synthetic $Ca_2Al_2SiO_7$ (gehlenite)-$Ca_2MgSi_2O_7$ (åkermanite) melilites. *Geochimica et Cosmochimica Acta* 45:1609–1617.

Chase M. W., Jr. 1998. NIST-JANAF thermodynamic tables, 4th ed. Monograph No 9. *Journal of Physical and Chemical Reference Data.*

Cohen R. E. 1981. Refractory inclusions in the Mokoia C3(V) carbonaceous chondrites (abstract). *Meteoritics* 16:304.

Davis A. M. and Grossman L. 1979. Condensation and fractionation of rare earths in the solar nebula. *Geochimica et Cosmochimica Acta* 43:1611–1632.

Davis A. M., MacPherson G. J., Clayton R. N., Mayeda T. K., Sylvester P. J., Grossman L., Hinton R. W., and Laughlin J. R. 1991. Melt solidification and late-stage evaporation in the evolution of a FUN inclusion from the Vigarano C3V chondrite. *Geochimica et Cosmochimica Acta* 55:621–637.

Ebel D. S. and Grossman L. 2000. Condensation in dust-enriched systems. *Geochimica et Cosmochimica Acta* 64:339–366.

El Goresy A. and Zinner E. K. 1994. Efremovka E49: A compact type A CAI containing a partially molten spinel-melilite-diopside xenolith (abstract). *Meteoritics* 29:461–462.

Fagan T. J., Krot A. N., and Keil K. 2000. Calcium, aluminum-rich inclusions in enstatite chondrites. *Meteoritics & Planetary Science* 35:771–783.

Fegley B., Jr., Post J. E., and Peck J. A. 1984. Mineral chemistry of a large spinel-rich inclusion in the Kaba CV3 chondrite (abstract). 15th Lunar and Planetary Science Conference. pp. 264–265.

Grossman L. 1972. Condensation in the primitive solar nebula. *Geochimica et Cosmochimica Acta* 36:597–619.

Grossman L. and Ganapathy R. 1976. Trace elements in the Allende meteorite: II. Fine-grained, Ca-rich inclusions. *Geochimica et Cosmochimica Acta* 40:967–977.

Grossman L., Fruland R.M., and McKay D.S., 1975. Scanning electron microscopy of a pink inclusion from the Allende meteorite. *Geophysical Research Letters* 2:37–40.

Grossman L., Ebel D. S., Simon S. B., Davis A. M., Richter F. M., and Parsad N. M. 2000. Major element chemical and isotopic compositions of refractory inclusions in C3 chondrites: The separate roles of condensation and evaporation. *Geochimica et Cosmochimica Acta* 64:2879–2894.

Hashimoto A. and Grossman L. 1985. SEM-petrography of Allende fine-grained inclusions (abstract). 16th Lunar and Planetary Science Conference. pp. 323–324.

Hashimoto A., Nishida M., and Hiyagon H. 2001. Four fine-grained inclusions in Yamato-81020 (abstract). *Meteoritics & Planetary Science* 36:A75–A76.

Holmberg B. B. and Hashimoto A. 1992. A unique, (almost) unaltered spinel-rich, fine-grained inclusion in Kainsaz. *Meteoritics* 27:149–153.

Huss G. R., MacPherson G. J., Davis A. M., Krot A. N., and Ulyanov A. A. 2002. Microdistribution of REE in fine-grained group II CAIs in Efremovka (abstract). *Meteoritics & Planetary Science* 37:A68.

Hutcheon I. D. 1982. The Mg isotopic composition of igneous-textured refractory inclusions from C3 meteorites (abstract). *Meteoritics* 17:230–231.

Kornacki A. S. 1981. Are CAIs condensates or distillation residues? Evidence from a comprehensive survey of fine- to medium-grained inclusions in the Allende C3(V) carbonaceous chondrites (abstract). 12th Lunar and Planetary Science Conference. pp. 462–464.

Kornacki A. S. 1982. Major and trace element fractionations in fine-grained CAIs: Evidence for igneous differentiation during melting induced by partial distillation (abstract). 13th Lunar and Planetary Science Conference. pp. 401–402.

Kornacki A. S. 1984. The mineralogy of spinel-rich Allende inclusions: Indicators of the oxidation state of the solar nebula (abstract). 15th Lunar and Planetary Science Conference. pp. 453–454.

Kornacki A. S. and Cohen R. E. 1983. On the origin of spinel-rich inclusions (abstract). 14th Lunar and Planetary Science Conference. pp. 393–394.

Kornacki A. S. and Fegley B., Jr. 1984. Origin of spinel-rich chondrules and inclusions in carbonaceous and ordinary chondrites. Proceedings, 14th Lunar and Planetary Science Conference. *Journal of Geophysical Research* 89:B588–B596.

Kornacki A. S. and Wood J. A. 1984. Petrography and classification of Ca, Al-rich and olivine-rich inclusions in the Allende CV3 chondrite. Proceedings, 14th Lunar and Planetary Science Conference. *Journal of Geophysical Research* 89: B573–B587.

Kornacki A. S. and Wood J. A. 1985. Mineral chemistry and origin of spinel-rich inclusions in the Allende CV3 chondrite. Mineral chemistry and origin of spinel-rich inclusions in the Allende CV3 chondrite. *Geochimica et Cosmochimica Acta* 49:1219–1237.

Krot A. N., Scott E. R. D., and Zolensky M. E. 1995. Mineralogic and chemical variations among CV3 chondrites and their components: Nebular and asteroidal processing. *Meteoritics* 30: 748–775.

Krot A. N., Petaev M. I., Scott E. R. D., Choi B. G., Zolensky M. E., and Keil K. 1998. Progressive alteration in CV3 chondrites: More evidence for asteroidal alteration. *Meteoritics & Planetary Science* 33:1065–1085.

Krot A. N., McKeegan K. D., Russell S. S., Meibom A., Weisberg M. K., Zipfel J., Krot T. V., Fagan T. J., and Keil K. 2001. Refractory Ca, Al-rich inclusions and Al-diopside-rich chondrules in the metal-rich chondrites Hammadah al Hamra 237 and QUE 94411. *Meteoritics & Planetary Science* 36:1189–1217.

Lin Y. and Kimura M. 1998. Anorthite-spinel-rich inclusions in the Ningqiang carbonaceous chondrite: Genetic links with type A and C inclusions. *Meteoritics & Planetary Science* 33:435–446.

Lin Y. and Kimura M. 2003. Ca-Al-rich inclusions from the Ningqiang meteorite: Continuous assemblages of nebular condensates and genetic link to type B inclusions. *Geochimica et Cosmochimica Acta* 67:2251–2267.

MacPherson G. J. and Grossman L. 1982. Fine-grained, spinel-rich, and hibonite-rich Allende inclusions (abstract). *Meteoritics* 17: 245–246.

MacPherson G. J. and Davis A. M. 1993. A petrologic and ion microprobe study of a Vigarano type B refractory inclusion; evolution by multiple stages of alteration and melting. *Geochimica et Cosmochimica Acta* 57:231–243.

MacPherson G. J. and Davis A. M. 1994. Refractory inclusions in the prototypical CM chondrite, Mighei. *Geochimica et Cosmochimica Acta* 58:5599–5625.

MacPherson G. J. and Huss G. R. 2000. Convergent evolution of CAIs and chondrules: Evidence from bulk compositions and a cosmochemical phase diagram (abstract #1796). 31st Lunar and Planetary Science Conference. CD-ROM.

MacPherson G. J. and Krot A. N. 2002. Distribution of Ca-Fe-silicates in CV3 chondrites: Possible controls by parent body compaction (abstract). *Meteoritics & Planetary Science* 37:A91.

MacPherson G. J., Wark D. A., and Armstrong J. T. 1988. Primitive material surviving in chondrites: Refractory inclusions. In *Meteorites and the early solar system,* edited by Kerridge J. F. and Matthews M. S. Tucson: University of Arizona Press. pp. 746–807.

MacPherson G. J., Petaev M. I., and Krot A. N. 2004. Bulk compositions of CAIs and Al-rich chondrules: Implications of the reversal of the anorthite/forsterite condensation sequence at low nebular pressures (abstract #1838). 35th Lunar and Planetary Science Conference. CD-ROM.

Mao X. Y., Ward B. J., Grossman L., and MacPherson G. J. 1990. Chemical compositions of refractory inclusions from the Vigarano and Leoville carbonaceous chondrites. *Geochimica et Cosmochimica Acta* 54:2121–2132.

Martin P. M. and Mason B. 1974. Major and trace elements in the Allende meteorite. *Nature* 249:333–334.

McGuire A. V. and Hashimoto A. 1989. Origin of zoned fine-grained inclusions in the Allende meteorite. *Geochimica et Cosmochimica Acta* 53:1123–1133.

Petaev M. I. and Wood J. A. 1998a. The condensation with partial isolation (CWPI) model of condensation in the solar nebula. *Meteoritics & Planetary Science* 33:1123–1137.

Petaev M. I. and Wood J. A. 1998b. The CWPI model of nebular condensation: Effects of pressure on the condensation sequence (abstract). *Meteoritics & Planetary Science* 33:A122.

Petaev M. I. and Wood J. A. 2000. The condensation origin of zoned metal grains in Bencubbin/CH-like chondrites: Thermodynamic model (abstract #1608). 31st Lunar and Planetary Science Conference. CD-ROM.

Petaev M. I., Wood J. A., Meibom A., Krot A. N., and Keil K. 2003. The ZONMET thermodynamic and kinetic model of metal condensation. *Geochimica et Cosmochimica Acta* 67:1731–1751.

Richter F. M., Liang Y., and Davis A. M. 1999. Isotope fractionation by diffusion in molten oxides. *Geochimica et Cosmochimica Acta* 63:2853–2861.

Robbie R. A. and Hemingway B. S. 1995. *Thermodynamic properties of minerals and related substances at 298.15 K and 1 bar (10^5 Pascals) pressure and at higher temperatures.* Bulletin 2131. Reston: U. S. Geological Survey.

Sack R. O. and Ghiorso M. S. 1994. Thermodynamics of multicomponent pyroxenes. III. Calibration of $Fe^{2+}(Mg)_{-1}$, $TiAl_2(MgSi_2)_{-1}$, $TiFe^{3+}{}_2(MgSi_2)_{-1}$, $AlFe^{3+}(MgSi)_{-1}$, $NaAl(Ca,Mg)_{-1}$, $Al_2(MgSi)_{-1}$, and $Ca(Mg)_{-1}$ exchange reactions between pyroxenes and silicate melts. *Contributions to Mineralogy and Petrology* 118:271–296.

Simon S. B. and Grossman L. 1997. In situ formation of palisade bodies in calcium, aluminum-rich refractory inclusions. *Meteoritics & Planetary Science* 32:61–70.

Simon S. B., Grossman L., and Davis A. M. 1991. Fassaite composition trends during crystallization of Allende type B refractory inclusion melts. *Geochimica et Cosmochimica Acta* 55:2635–2655.

Simon S. B., Davis A. M., and Grossman L. 1998. Formation of an unusual compact type A refractory inclusion from Allende. *Meteoritics & Planetary Science* 33:115–126.

Stolper E. M. 1982. Crystallization sequences of Ca-Al-rich inclusions from Allende: An experimental study. *Geochimica et Cosmochimica Acta* 46:2159–2180.

Sylvester P. J., Grossman L., and MacPherson G. J. 1992. Refractory inclusions with unusual chemical compositions from the Vigarano carbonaceous chondrite. *Geochimica et Cosmochimica Acta* 56:1343–1363.

Sylvester P. J., Simon S. B., and Grossman L. 1993. Refractory inclusions from the Leoville, Efremovka, and Vigarano C3V chondrites: Major element differences between types A and B, and extraordinary refractory siderophile element compositions. *Geochimica et Cosmochimica Acta* 57:3763–3784.

Tanaka T. and Masuda A. 1973. Rare-earth elements in matrix, inclusions, and chondrules of the Allende meteorite. *Icarus* 19: 523–530.

Ulyanov A. A. 1984. On the origin of fine-grained Ca, Al-rich inclusions in the Efremovka carbonaceous chondrite (abstract). 15th Lunar and Planetary Science Conference. pp. 872–873.

Wark D. A. 1987. Plagioclase-rich inclusions in carbonaceous chondrite meteorites: Liquid condensates? *Geochimica et Cosmochimica Acta* 51:221–242.

Wark D. A., Kornacki A. S., Boynton W. V., and Ulyanov A. A. 1986. Efremovka fine-grained inclusion E14: Comparisons with Allende (abstract). 17th Lunar and Planetary Science Conference. pp. 921–922.

Wood J. A. and Hashimoto A. 1993. Mineral equilibrium in fractionated nebular systems. *Geochimica et Cosmochimica Acta* 57:2377–2388.

Yoneda S. and Grossman L. 1995. Condensation of CaO-MgO-Al_2O_3-SiO_2 liquids from cosmic gases. *Geochimica et Cosmochimica Acta* 59:3413–3444.

APPENDIX

Thermodynamic Analysis

We can explore physicochemical conditions of the mineral reactions observed in the fine-grained, spinel-rich CAIs by modeling the metasomatic interaction of solid inclusions injected into a system with solar bulk composition. The residual gaseous phase of such a system is assumed to be in equilibrium with the solid phases condensed out of the system. We further assume an open-system type of interaction between the fine-grained CAIs and the surrounding gaseous phase, i. e., the amounts Si, Mg, Ca, H, and O added to or subtracted from the CAIs by Reactions 1–10 do not change the partial pressures of Ca, Mg, SiO, H_2O, and H_2 in the gaseous system due to the very low mass ratio of CAIs to the gaseous phase. The chemical compositions of the residual gaseous phase are calculated using the CWPI code (Petaev and Wood 2000; Petaev et al. 2003).

The equations linking the equilibrium constants ($logK_i$) of Reactions 1–10 with the partial pressures of gaseous species (log[Mg], log[SiO], log[H_2O/H_2], and log[Ca]) and the activities of end members of clinopyroxene (log[Di], log[CATS]) and melilite (log[Gel], log[Åk]) mineral solid solutions are as follows (Since the activities of pure spinel and anorthite are equal to unity, the corresponding terms are omitted from Equations 11–20.):

$$\log K_1 = \log(Di) + \log(CATS) - \log(Gel) - \log(Mg) - 2\log(SiO) - 3\log(H_2O/H_2) \quad (11)$$

$$\log K_2 = 2\log(Di) + 4\log(CATS) - 3\log(Gel) - 5\log(SiO) - \log(Mg) - 6\log(H_2O/H_2) \quad (12)$$

$$\log K_3 = \log(Di) - \log(Gel) - \log(Mg) - 3\log(SiO) - 4\log(H_2O/H_2) \quad (13)$$

$$\log K_4 = \log(Gel) - \log(CATS) - \log(Di) + \log(Mg) + 2\log(SiO) + 3\log(H_2O/H_2) \quad (14)$$

$$\log K_5 = 3\log(Gel) - 4\log(CATS) - 2\log(Di) + 5\log(SiO) + \log(Mg) + 6\log(H_2O/H_2) \quad (15)$$

$$\log K_6 = \log(Gel) - \log(Di) + 3\log(SiO) + \log(Mg) + 4\log(H_2O/H_2) \quad (16)$$

$$\log K_7 = \log(Gel) + \log(Åk) - 4\log(Di) + 4\log(Mg) + 5\log(SiO) + 9\log(H_2O/H_2) \quad (17)$$

$$\log K_8 = 2\log(Gel) + \log(Åk) - 5\log(Ca) - 2\log(SiO) - 7\log(H_2O/H_2) \quad (18)$$

$$\log K_9 = 2\log(Gel) + \log(Di) - 4\log(Ca) - 2\log(SiO) - 6\log(H_2O/H_2) \quad (19)$$

$$\log K_{10} = 2\log(Gel) + \log(Mg) - 3\log(Ca) - 2\log(H_2O/H_2) \quad (20)$$

The numerical values of the equilibrium constants of Reactions 1–10 were calculated using the thermodynamic database of the CWPI code. The values of standard thermodynamic properties of minerals and gaseous species involved in Reactions 1–10 are from Chase (1998), Berman (1988), Sack and Ghiorso (1994), and Robbie and Hemingway (1995). The melilite solid solution was treated as non-ideal (Charlu et al. 1981). Ignoring small amounts of $MgAl_2SiO_6$, $CaTi^{4+}Al_2O_6$, and $CaTi^{3+}AlSiO_6$, the clinopyroxene was treated as an ideal solution of Ca-Tschermakite (CATS, $CaAl_2SiO_6$) and diopside ($CaMgSi_2O_6$) (Sack and Ghiorso 1994). Calculations were done in the temperature range of 1000– 1600 K and the pressure range of 10^{-3}–10^{-8} bar.

The results of the thermodynamic analysis are shown in Figs. 17–19 as the log P versus T plots. In calculating the positions of phase boundaries on these plots, all parameters of Equations 11–20 were replaced with numerical values either calculated using the CWPI code (partial pressures of gaseous species) or measured in the fine-grained inclusions studied. The compositions of mineral solid solutions used in the analysis are Al-rich melilite ($Ge_{95}Åk_5$), Al-poor diopside ($Di_{95}CATS_5$), and Al-enriched diopside ($Di_{80}CATS_{20}$).

The phase boundaries of the alteration Reactions 1–3 are shown in Fig. 18 along with that of the reaction reciprocal to Reaction 10. The latter also might have been involved in the process of melilite alteration; in fact, this is the only reaction that results in evaporative loss of Ca from the primary

melilite-spinel assemblage. The melilite stability fields are on the right-hand side of all phase boundaries. The condensation curve of forsterite that shows that the alteration of melilite occurs before the appearance of forsterite is also plotted, which is consistent with the lack of forsterite in the inclusion rims. Two possible scenarios of melilite alteration can be considered: 1) alteration during continuous cooling, and 2) isothermal alteration. Since all phase boundaries are essentially parallel to each other, the alteration sequence is independent of nebular pressure, although the absolute temperatures of the reactions do depend on pressure. Let us consider what happens to the the primary melilite-spinel assemblage in each scenario at the representative nebular pressure of 10^{-6} bar.

In the most plausible Scenario 1, the formation of Al-diopside by Reaction 2 begins at ~1286 K (Fig. 18a) at the melilite-spinel interface. As the reaction proceeds, the Al-content in clinopyroxene increases with falling temperature until decomposition of melilite into anorthite and spinel by the inverse of Reaction 10 commences at 1275 K. The Ca loss from the inclusions begins. Both reactions continue until Reaction 1 becomes possible at ~1271 K. Reaction 3 becomes possible at 1261 K, just before the cessation of alteration at ~1260 K when the concentration of the diopsidic end member drops to 80 mol% (Fig. 18b). Thus, Reaction 3 is not an important source of anorthite and diopside. At lower temperatures, the residual melilite will continue to decompose into anorthite and spinel until complete disappearance of the former. Indeed, the exhaustion of melilite at any stage would stop the alteration.

In an isothermal Scenario 2, the sequence of alteration depends on the temperature of the ambient nebular gas in which the primary melilite-spinel assemblage is injected. In the temperature range of 1275–1286 K, Reaction 2 will start at the melilite-spinel interface and will proceed until the concentration of diopside reaches the equilibrium value (~90 mol% at 1275 K). No anorthite will be formed. In the temperature range of 1271–1275 K, both Reaction 2 and the inverse of Reaction 10 will proceed simultaneously. Formation of clinopyroxene will cease when the equilibrium concentration of Di is reached (~88 mol% at 1271 K), while the formation of anorthite and spinel will continue until melilite disappears completely. At lower temperatures, all reactions will take place until melilite disappears. The measured concentrations of the Di end member in clinopyroxenes suggest that the alteration temperature should not be lower than ~1260 K (Fig. 18b); otherwise, more aluminous clinopyroxene would have formed.

The phase boundaries of reactions relevant to the formation of melilite-rich mantles of the zoned inclusions by the evaporative loss of Mg and/or Si (direct or reciprocal Reactions 4–8) are shown in Fig. 19 along with the reference condensation curve of forsterite. Again, the stability fields of melilite are on the right-hand sides of the phase boundaries. The phase boundaries of Reactions 7 and 8 lie deep within the stability field of forsterite, which makes these reactions irrelevant because the lack of forsterite in the inclusions points to much higher alteration temperatures (above the condensation temperatures of forsterite). The sequence of evaporation Reactions 4–6 is essentially reciprocal to the sequence of alteration reactions described in the alteration Scenario 1.

At a nebular pressure of 10^{-6} bar, the formation of melilite starts at ~1260 K from clinopyroxene, spinel, and anorthite through Reactions 4–6 (Fig. 19a). Soon after (1261 K), the anorthite disappears (Reaction 6 in Fig. 19b). Further evaporation will result in formation of melilite ± spinel from clinopyroxene through Reactions 4 and 5. This makes Reaction 10 metastable, i.e., it can proceed only if the inclusions were heated to ~1275 K so rapidly that the anorthite has not been exhausted due to the slower kinetics of Reaction 6. Reaction 9 (not shown) cannot proceed as written because anorthite disappears well before the formation of melilite through this reaction and becomes thermodynamically favorable. Above 1271 K, clinopyroxene decomposes into melilite and spinel through Reaction 6. The inclusions must have been removed from the contact with hot nebular gas at ~1285 K to preserve measured Al contents in clinopyroxenes.